On the Hydrodynamic Stability of an Imploding Rotating Circular Cylindrical Liquid Liner

E.J. Avital[1*], V Suponitsky[2], I.V. Khalzov[2], J Zimmermann[2] and D Plant[2]

[1]School of Engineering and Materials Science, Queen Mary University of London

327 Mile Road London E1 4NS, UK

[2]General Fusion Inc., 106-3680 Bonneville Pl, Burnaby, BC, V3N 4TS, Canada

Abstract

The hydrodynamic stability of an imploding cylindrical liquid liner is analytically and numerically investigated. Such dynamic system can be used to compress gas trapped by the liner, as one may seek in a hydrogen fusion reactor. For such system it is vital for the liner to stay intact at least up to the turnaround point, which marks the point of maximum compression of the inner gas. New two-dimensional linear stability of Bell-type equation and Wentzel-Kramers-Brillouin (WKB) approximations are derived to account for the rotation of the liner. Excellent agreement is achieved between CFD and 1D analysis for the trajectory of the unperturbed liner. Very good agreement is also achieved between the Bell type linear stability solution and the CFD until non-linear effects take hold near the turnaround point. The WKB approximation also agrees well but only at the early stage of the liner motion. Viscosity, surface tension and inner gas stability waves are found to have a small effect for a liner's radial compression of up to ten.

It is seen that the rotation has little effect on the perturbation amplitude during the accelerating stage of the liner, which is dominated by a slow oscillatory growth of a Bell-Plesset type at the studied conditions. However, at the decelerating stage towards the turnaround point, Rayleigh-Taylor rapid perturbation growth is suppressed at sufficiently large rotation rates. Hence, when coupled with non-linear saturation effects, the liner stays much intact until the turnaround point for radial compression ratios of up to ten. New simple linear stability limits are derived and are analysed.

Keywords: Imploding cylindrical liner, linear stability, Rayleigh-Taylor, rotation, perturbation suppression,

* Corresponding author; email: e.avital@qmul.ac.uk

List of symbols:

$\mathcal{A}$ – Atwood number; $(\rho-\rho_{in})/(\rho+\rho_{in})$

a_c – centripetal acceleration at the liner's inner surface

a_t – effective centripetal acceleration at the liner's inner surface

c_{in} – inner gas speed of sound

L – angular momentum

m – polar mode number

p – pressure, i.e. $p = p^0 + p'$

p^0 – unperturbed pressure

p' – perturbation pressure

R_{in} – the radial location of the liner inner surface

R_{out} – the radial location of the liner outer surface

r – radial distance

t – time

$S=R_{in}/R_{out}$

u – velocity, i.e. $u = u^0 + u'$

u^0 – unperturbed velocity

u' – perturbation velocity

V – radial velocity of liner inner surface, i.e. dR_{in}/dt

V_0 – initial radial velocity of liner inner surface, i.e. dR_{in}/dt at t=0

ϕ – perturbation velocity potential in the liner

ϕ_{in} – perturbation velocity potential in the inner gas

η – surface perturbation

η_a – surface perturbation polar mode

γ – specific heat ratio

θ – polar angle

σ – surface tension coefficient

ρ – incompressible liner density

ρ_{in} – compressible inner gas density

Ω – unperturbed rotational speed of the liner

Ω_0 – unperturbed initial rotational speed of the liner inner surface

Ω_∞ – unperturbed initial rotational speed of the liner at formal limit $r \to \infty$

ω – perturbation frequency and $\overline{\omega} \equiv \omega + m\Omega$

1. Introduction

The flow of liquid in the form of a circular cylindrical shell can be found in a wide range of dynamic systems from problems of drainage, mechanical bearing, off-shore structures (Wang et al. 2018), co-axial jets to liners used to shield an interior object or to compress an interior gas (Huneault et al. 2019). The focus of this study is the liner used to compress interior gas as in a prototype of a fusion reactor system (Turchi 2017a). By considering compression of the gas, rather than a plasma target (as in a fusion reactor), we omit additional magnetohydrodynamic (MHD) effects during implosion of the liner. Achieving energy generation using nuclear hydrogen fusion has attracted significant attention and effort since the 50's of the last century. However, it still has to produce energy in a commercially viable way. The use of the liquid metal liner to compress plasma target is part of the magnetized target fusion (MTF) approach, where both magnetic fields and mechanical forces are used to compress the plasma containing the hydrogen fuel until sufficient high temperature and pressure are achieved for fusion to occur. It is a mixture of two systems; the magnetic confinement fusion (MCF) and the inertial confinement fusion (ICF). MCF is based on torodial machines as tokamaks that squeeze the plasma and thus raising its temperature as required for fusion. ICF heats and compresses the plasma using usually high energy lasers. Both approaches requires large facilities as the ITER in South France for the MCF. The MTF combines magnetic confinement and mechanical compression and thus can be deployed in much smaller facilities, see Suponitsky et al (2014, 2107) for further details.

The MTF approach has the promise of a reduced cost and system's size, but still has to overcome technical challenges that are inherent to such a dynamic system with requirements of very short time scales due to the short life span of the plasma. One of the challenges is to keep the metal liner intact with no significant deformation until at least the plasma has been sufficiently compressed (Barcilon et al. 1974). A typical liner is in the form of a circular cylindrical shell whose cross-section is illustrated in Fig. 1 or in the form of a spherical shell. The focus of this study is on the circular cylindrical shell, where ideally it should go through a cycle of first radially converging inwards (compressing the inner gas) until a turnaround point is reached and the liner changes its radial direction of motion and starts diverging outwards approaching the starting point of the cycle (Barcilon et al. 1974, Turchi 2017a).

In the 1970s as part of the Linus project, the liner was proposed to be pushed by an axial magnetic field, which led to the onset of Rayleigh-Taylor instability (RTI) capable of breaking down the liner during the implosion. This instability is triggered when a lighter fluid pushes the heavier fluid

as in the case of a layer of water above a layer of air. It can be found in a wide range of applications from oceanic and atmospheric stratification flows to jet atomisation (Kull 1991). Rotating the liner was found to reduce RTI, in particular, two-dimensional liner stability analysis of a liner driven by an axial magnetic field has revealed that the rotational energy has to be at least 60% of the total liner energy in order to avoid RTI (Barcilon et al. 1974). This can have a significant effect on the ability to achieve highly compressed plasma at the turnaround point.

Increasing the initial thickness of the liner can also decrease RTI effect in the linear stability sense (Barcilon et al. 1974), and also in non-linear stability sense. This is because of the instability saturation in the non-linear stage of the RTI (Kull 1991). Hence, the thick liner does not break down, but it can still lead to a reduced uniform compression of the plasma (Turchi 2017a). High rotation and/or an initially thick liner can also reduce the compression efficiency of the plasma by increasing the radius of the turnaround point and increasing the time required to reach the turnaround point, thus caution must be applied to chose the right level of rotation and thickness (Book & Winsor 1974). The ability of rotation to reduce RTI was later confirmed by a set of experimental flow visualisations, showing the need for the effective centripetal acceleration to be negative (Turchi et al. 1976). This was also recently demonstrated in the experiments of Huneault et al. (2019), showing that rotation can suppress low mode number perturbations RTI growth, leading to geometrical growth instead.

Another way to reduce RTI is to push the liner using an array of circular pistons (Turchi et al. 1977). It can suppress feed-through RTI effects by preventing perturbation growth on the outer side of the liner as is analysed in this study. The liquid liner's motion is assumed as of incompressible flow following Barcilon et al. (1974), Kull (1991), Turchi et al. (1976) and Velikovich & Schmit (2015). When the compression level is extremely high, it may reach the level of the liquid's bulk modulus causing compressibility to mildly slow down the motion and reduce the transfer of the liner's kinetic energy towards the compression of the inner gas (the plasma) (Book and Turchi, 1979). Such case is left for a future study.

An innovative dynamic system of steam-driven pistons transmitting an acoustic pulse into the liner and causing it to implode was analysed by Suponitsky et al. (2017), showing a significant uniform compression of the plasma near the turnaround point. However, energy losses during the acoustic pulse transfer and very strict synchronization requirements can put significant constraints on this kind of system. An alternative design, based on a single switch of high compression gas to push the

liner, was analysed by Avital et al. (2017). As in the case of the highly compressed liner near the turnaround point, it yielded a fluid hammer phenomenon of a return azimuthal pressure wave that increased compression forces over the liner but reduced the compression uniformity. A third and slower system was suggested by Suponitsky et al. (2018), in a form of a rotating turbine-like drum with radially-tilted blades filled with liquid between them. The drum then was rapidly decelerated, causing the liquid to radially flow inwards and form a rotating liner converging towards the centre. Experiments using water and complementary computational fluid dynamics (CFD) have shown the ability of such a system to achieve a stable cylindrical imploding liner when the effective radial acceleration is noticeably negative.

The subject of this study is the hydrodynamics of an imploding cylindrical liner pushed by pistons, where the analysis of the kind of pistons is left to other studies. The focus here is on the motion and stability of the cylindrical liner system. A similar system was also recently experimentally investigated by Huneault et al. (2019), where the main focus was to provide experimental demonstration that sufficient rotation of the liner can suppress RTI during decelerating stage of the liner and after the turnaround point. New linear stability analysis is presented which includes the effect of rotation and instability waves in the inner compressed gas. Two approaches of stability analysis are used. The first approach is deriving an exact (in the linear sense) hydrodynamic stability equation of the Bell type as was done by Mikaelian (2005) for liners with infinite outer radii but adding the effect of rotation. Hence, this approach approximates the instability process in thick liners. The second approach is the Wentzel-Kramers-Brillouin (WKB) approximation previously used by Velikovich & Schmit (2015) in a detailed study for the case of non-rotating liner and no aerodynamic instability waves in the compressed gas. The approximation is in the assumption that development of the instability wave occurs in a much faster time scale compared to that of the liner's radial motion. Two-phase CFD simulations using the OpenFoam software are also performed to complement the analysis by providing further comparison for the linear stability analysis results and looking at non-linear effects of the perturbation development.

In both forms of the stability analysis and the CFD computations, the perturbation is assumed as two-dimensional as in the stability analysis of Barcilon et al. (1974), Mikaelian (2005) and Epstein (2004). Extension for 3D instability wave is readily possible, particularly in the WKB approximation where a Bessel function expansion can be used (Velikovich & Schmit 2015, Vadivukkarasan & Panchagnula 2019). However, the 2D instability assumption already captures the main features of the stability process in terms of the liner's acceleration. It also allows deriving a

simple limit for Rayleigh-Taylor (RT) stability beyond the known limit of a negative effective centripetal acceleration at the turnaround point and significantly reduces the computational cost of the CFD computations. Hence, 3D stability analysis is left for a future study.

2. Methodology

A circular cylindrical liner is assumed, where its cross-section is illustrated in Fig. 1. The liner motion is assumed to experience pressures that do not lead to strong compression and refraction waves and, hence, liquid liner is assumed incompressible, while the inner gas is compressible for the 1D unperturbed motion analysis (Barcilon et al. 1974, Velikovich & Schmit 2015). The outer surface of the liner is assumed to be exposed to a pressure p^0_{out} carried by a ring of pistons and thus the surface perturbation can only exist on the inner surface of the liner. The 1D equation of motion is derived for the unperturbed liner motion. It is followed by linear stability analysis accounting for hydrodynamic forces and rotation inside the liner. Finally the methodology of the complementary CFD computations is presented.

2.1 Equation of motion of the unperturbed liner

The momentum equation in the radial direction while assuming perfect symmetry and no motion in the axial direction is:

$$\frac{\partial u_r^0}{\partial t}+u_r^0\frac{\partial u_r^0}{\partial r}-\frac{(u_\theta^0)^2}{r}=-\frac{1}{\rho}\frac{\partial p^0}{\partial r} \quad , \tag{1}$$

where $u^0_r = (R_{in}\, dR_{in}/dt)/r$ due to incompressibility, $u^0_\theta=\Omega(r)r$ and the angular momentum $L= ru^0_\theta$ is preserved during motion. The superscript 0 denotes an unperturbed property. Eq. (1) converges to the known non-rotating liner equation of motion when $u^0_\theta=0$ (Kull 1991, Velikovich & Schmit 2015) and to the base flow for rotational flow stability analysis (Drazin and Reid 2004). It should be also noted, that because ru^0_r is constant in space due to continuity, the viscous term is exactly zero in the 1D radial Navier-Stokes equation and, hence, it does not appear in Eq. (1). Following the derivations of Kull (1991) for a non-rotating liner and Suponitsky et al. (2018) for a rotating liner, while neglecting surface tension, one gets the equation of motion as:

$$\left[R_{\text{in}}\frac{d^2R_{\text{in}}}{dt^2}+V^2\right]\ln\frac{1}{S}-\frac{V^2}{2}\left(1-S^2\right)=-\frac{p^0_{out}-p^0_{\text{in}}}{\rho}+\int_{R_{\text{in}}}^{R_{out}}\frac{L^2}{r^3}dr \quad , \tag{2}$$

where

$$V(t)\equiv\frac{dR_{\text{in}}}{dt}\ , \quad S(t)=\frac{R_{\text{in}}}{R_{out}}\ , \quad L(r,t)=r^2\Omega(r,t) \quad . \tag{3}$$

It is shown in Section 2.2.1 that a particular distribution of an angular momentum is required to ensure potentiality of velocity perturbation (Eqs. 13, 14):

$$L(r,t)=a(t)r^2+b(t),$$

where coefficients a(t) and b(t) are determined by initial rotation profile and by the compression trajectory of liner (due to conservation of angular momentum). Cases of a particular interest are liner initially rotating as a solid body (mainly studied in the work), and as a potential vortex. Distributions of angular momentum for those two cases are given by

$$L_{solid\ \ body}(r,t)=\Omega_0\left(r^2-R_{\text{in}}^2(t)+R_{\text{in}}^2(0)\right) \quad \text{and} \quad L_{potential\ \ vortex}(r,t)=\Omega_0 R_{\text{in}}^2(0).$$

In order to solve Eq. (2) for inner liner surface radius R_{in}, initial conditions for the liner motion have to be provided. Here it is assumed that liner is initially at rest (with respect to the radial motion component) and starts to implode due to a sudden increase of external pressure. For this case the initial conditions are $S(0)=R_{in}(0)/R_{out}(0)$ and $V(0)=0$ along with the mass conservation requirement of $R^2_{out}(t)-R^2_{in}(t) = R^2_{out}(0)-R^2_{in}(0)$. Alternatively, one can consider a liner that already has some initial radial velocity. In this case $V(0)=V_0$, where V_0 is initial radial velocity of the inner surface. However, one should keep in mind that if liner's initial radial velocity is not zero, initial rotation of the liner can not be prescribed as a solid body rotation. Hence, the initial radial distribution of the angular momentum in the liner should be provided.

Temporal pressure distribution acting on the inner and outer surfaces of the liner should be also provided in order to solve Eq. (2). Assuming isentropic compression of the inner gas;

$$\frac{p_{\text{in}}^0(t)}{p_{\text{in}}^0(0)}=\left[\frac{\rho_{\text{in}}(t)}{\rho_{\text{in}}(0)}\right]^{\gamma}=\left[\frac{R_{\text{in}}(0)}{R_{\text{in}}(t)}\right]^{2\gamma} \quad . \tag{4}$$

Taking $\gamma=2$ will mimic the effect of a magnetic pressure due to an inner magnetic field (Velikovich & Schmit 2015). Temporal outer pressure distribution is determined by the system used to implode the liner, and can be nearly constant, pulse shaped etc.. Increase in the rotational speed of the liner with all other parameters in Eq. (2) kept unchanged, delays the occurrence of the turnaround point and increases liner's minimum radius. It also increases the dwell time at the turnaround point and leads to a more gradual re-bounce. Thus, if the same temporal outer pressure is applied for different initial rotational speeds of the liner, the different implosion trajectories of the liner are obtained. The goal of this work is to identify the pure effect of rotation on the stability process, hence, it is argued, that liners of the same geometry and trajectory but with different rotational speeds should be compared.

This can be done by adjusting the temporal outer pressure distribution acting on the liner. By taking the trajectory of the non-rotating liner as the one that all other liners should follow, the outer pressure required to achieve the same trajectory for different rotational speeds can be calculated as:

$$p^0_{\text{out}}(L,t) = p^0_{\text{out}}(L=0,t) + \rho \int_{R_{\text{in}}(t)}^{R_{\text{out}}(t)} \frac{L^2(r,t)}{r^3} dr \quad . \tag{5}$$

This means the outer pressure should be increased for higher rotational speeds in order to overcome the centrifugal force expressed by the last term in Eq. (5). For the cases considered in this study, a constant outer pressure has been taken for a non-rotating liner and then Eq. (5) has been used to calculate the required temporal pressure profile at different rotational speeds.

In Eq. (2) it was assumed that the pressure of the liner at $r=R_{out}$ is equal to the outer pressure p^0_{out} and $p=p^0_{in}$ at $r=R_{in}$. If the surface tension is accounted then the relation is (Drazin and Reid 2004):

$$p^0_{\text{liner}}(r=R_{\text{out,in}}) = p^0_{\text{out,in}} \pm \frac{\sigma}{R_{\text{out,in}}} \quad , \tag{6}$$

where the plus sign is for the outer surface and the minus sign is for the inner surface. Typical values of σ is 0.072 N/m for water-air interface and 0.38 N/m for liquid lithium-air around a temperature of 500 K. R_{in} is in the order of 1 cm. Hence, the effect of the surface tension on the unperturbed motion is very small as compared to p^0_{out} of 5 bars or more and can be neglected as done by Kull (1991), Velikovich & Schmit (2015) and Suponitsky et al. (2018). The numerical results in Section 3 have shown that the effect of the surface tension on the unperturbed motion and the perturbation development of the liner can be neglected as further discussed in Section 3.3.

Eq. (2) was solved for R_{in} using a 4^{th} order Runge-Kutta method. Numerical convergence was checked by varying number of points across the thickness of the liner and the time step of the Runge-Kutta method.

2.2 Liner linear stability analysis

Two approaches are used: the Bell-type stability equation and the WKB approximation. Both have their merits and drawbacks, while both account for the rotational effect that includes both the centrifugal and Coriolis forces in the linear sense using the linearly perturbed cylindrical Euler equations (Drazin and Reid 2004). The WKB approximation assumes that the development of the liner motion and its perturbation operate at different time scales, therefore the stability analysis is carried out assuming a liner frozen in time, yielding a wave growth rate that varies in time when assuming an exponential time solution. This is obviously an approximation, particularly at time stages near the turnaround point where rapid changes can occur within the liner's trajectory. On the

other hand, this approach is well established (Barcilon et al. 1974, Velikovich & Schmit 2015) and can be easily extended to include stability waves inside the inner gas as done in this study. The derivation of the Bell-type stability equation is exact in the linear sense, but it is not straight forward to include the inner gas perturbations. Hence, it will be assumed the Atwood number is one in the derivation, $\mathcal{A}$=1. Later it will be observed in Section 3 that the effect of the inner gas perturbations is small for the studied cases.

In both derivations presented in this study, viscous and surface tension forces are not accounted as in previous stability analyses for liners with no rotation or with no perturbations in the inner gas (Barcilon et al. 1974, Epstein 2004, Mikaelian 2005, Velikovich & Schmit 2015). Both effects tend to stabilise the motion as the polar wave number m increases (Avital 1995, Drazin and Reid 2004). However, the very small time scale of the liner motion in the examples studied here, means that viscous effects do not have sufficient time to affect the perturbation's growth as is confirmed by the complementary CFD computations and the scaling analysis in Section 3.3. The surface tension increases the effective unperturbed pressure gradient in the WKB approximation and thus makes the effective centripetal acceleration more negative for the stability process. Hence, it can increase the 2D stability as was also experimentally observed by Huneault et al. (2019). For non-rotating 3D liners the surface tension can cause 3D long wave axial and helical instabilities as found using the WKB approximation (Vadivukkarasan & Panchagnula 2019). However, again the effect of the surface tension was found to be small for the investigated rotating 2D liners as evident from the CFD computations and the scaling analysis in Section 3.3 and thus it is left for a future study. Finally, it is worth re-iterating that linear stability analysis in the paper is limited to the azimuthal perturbation only, with the effect of liner rotation on the axial perturbations is left for the future work.

2.2.1 The Bell-type stability equation

Here we derive the Bell-type equation for linearized dynamics of liner surface perturbation η when the outer radius of liner is infinite. We restrict our derivation to the case of perturbations with no z-dependence and assume Atwood number $\mathcal{A}$=1 during the entire implosion. As usual in linearized analysis, perturbations with different polar mode numbers m (i.e., different Fourier harmonics $e^{im\theta}$) can be treated separately since they are decoupled.

First, we consider the velocity perturbation in the liner and derive its relation with pressure perturbation. The perturbation of liner velocity is assumed to be potential and incompressible. It is

worth noting, that the assumption of potential flow is fully justified for a non-rotating liner, as in this case flow can be assumed to be both inviscid (as the small time scale of the motion renders viscous effects negligible) and irrotational (as the motion departs from rest, which by Kelvin's theorem, gives an irrotational flow). For the initially rotating liner, however, certain limitation on angular momentum distribution is applied, as discussed farther in this section. As such:

$$\vec{u}\,' = \nabla \phi, \qquad \nabla^2 \phi = 0. \tag{7}$$

In polar coordinates, the solution for potential that decays at infinity is

$$\phi = B(t) r^{-m} e^{im\theta}, \qquad m > 0. \tag{8}$$

Taking into account that

$$(\vec{u}\cdot\nabla)\vec{u} = \nabla \frac{\vec{u}^2}{2} - \vec{u}\times(\nabla\times\vec{u}),$$

we can write the linear part of the perturbed Navier-Stokes equation as

$$\frac{\partial \vec{u}\,'}{\partial t} + \nabla(\vec{u}^0\cdot\vec{u}\,') - \vec{u}\,'\times(\nabla\times\vec{u}^0) - \vec{u}^0\times(\nabla\times\vec{u}\,') + \nabla\frac{p'}{\rho} = 0. \tag{9}$$

Here prime denotes the perturbed part of corresponding variable, and

$$\vec{u}^0 = u_r^0 \vec{e}_r + u_\theta^0 \vec{e}_\theta = \frac{R_{\text{in}}(t)}{r}\frac{dR_{\text{in}}(t)}{dt}\vec{e}_r + r\,\Omega(r,t)\vec{e}_\theta. \tag{10}$$

is the unperturbed velocity. For potential velocity perturbation this becomes:

$$\nabla\left(\frac{\partial\phi}{\partial t} + \vec{u}^0\cdot\nabla\phi + \frac{p'}{\rho}\right) - \nabla\phi\times(\nabla\times\vec{u}^0) = 0. \tag{11}$$

In order for velocity perturbation to stay potential during dynamics described by Eq. (11), the last term in this equation should be a full gradient, i.e., the curl of it should be zero. Since unperturbed vorticity is

$$\vec{\omega}^0 \equiv \nabla\times\vec{u}^0 = \frac{1}{r}\frac{\partial(ru_\theta^0)}{\partial r}\vec{e}_z,$$

the condition for potentiality of velocity perturbation is

$$\nabla\times(\nabla\phi\times\vec{\omega}^0) = -(\nabla^2\phi)\vec{\omega}^0 - (\nabla\phi\cdot\nabla)\vec{\omega}^0 = -\frac{\partial\phi}{\partial r}\frac{\partial}{\partial r}\left(\frac{1}{r}\frac{\partial(ru_\theta^0)}{\partial r}\right)\vec{e}_z = 0. \tag{12}$$

This condition requires that profile of unperturbed angular momentum stays quadratic in radius at all times t (including t=0), namely,

$$L(r,t) \equiv ru_\theta^0 = r^2\Omega(r,t) = a(t)r^2 + b(t), \tag{13}$$

where coefficients $a(t)$ and $b(t)$ are determined by initial rotation profile and by compression trajectory of the liner (due to conservation of angular momentum), so that:

$$a(t) = \Omega_\infty, \qquad b(t) = \Omega_0 R_{\text{in}}^2(0) - \Omega_\infty R_{\text{in}}^2(t), \tag{14}$$

with Ω_0 and Ω_∞ being initial (at time t=0) angular velocities at inner liner surface and at infinity, respectively. For such angular momentum profile, the vorticity is given by

$$\vec{\omega}^0 = 2\Omega_\infty \vec{e}_z,$$

and the last term in Eq. (11) then becomes:

$$-\nabla\phi\times(2\Omega_\infty \vec{e}_z) = -2\Omega_\infty\left(\frac{im\phi}{r}\vec{e}_r + \frac{m\phi}{r}\vec{e}_\theta\right) = \nabla(2i\Omega_\infty\phi). \tag{15}$$

Here we used the fact that for ϕ given by Eq. (8)

$$\frac{\partial\phi}{\partial r} = -\frac{m\phi}{r}, \qquad \frac{\partial\phi}{\partial\theta} = im\phi.$$

Removing gradient in Eq. (11), we obtain:

$$\frac{\partial\phi}{\partial t} - \frac{mR_{\text{in}}}{r^2}\frac{dR_{\text{in}}}{dt}\phi + im\Omega\phi + 2i\Omega_\infty\phi + \frac{p'}{\rho} = 0. \tag{16}$$

From this equation we can find the pressure perturbation p' at r=R_{in}:

$$p'(R_{\text{in}}) = \frac{\rho}{R_{\text{in}}^m}\left(-\frac{\partial B}{\partial t} + \frac{mB}{R_{\text{in}}}\frac{dR_{\text{in}}}{dt} - im\Omega_{\text{in}}B - 2i\Omega_\infty B\right)e^{im\theta}, \tag{17}$$

where Ω_{in} is the angular velocity at the inner liner surface (due to angular momentum conservation):

$$\Omega_{\text{in}}(t) = \Omega_0\frac{R_{\text{in}}^2(0)}{R_{\text{in}}^2(t)}.$$

The perturbation of liner velocity is related to the surface perturbation by the kinematic boundary condition. If the radius of perturbed surface is given by

$$R(\theta,t) = R_{\text{in}}(t) + \eta(\theta,t),$$

then the kinematic boundary condition is

$$u_r|_R = \left.\frac{dR}{dt}\right|_R \equiv \left.\left(\frac{dR_{\text{in}}}{dt} + \frac{\partial\eta}{\partial t} + \Omega\frac{\partial\eta}{\partial\theta}\right)\right|_R, \tag{18}$$

where u_r is the full perturbed radial component of velocity

$$u_r = u_r^0 + \frac{\partial\phi}{\partial r},$$

and all quantities are evaluated at perturbed surface R. Taylor expansion of Eq. (18) up to linear terms in perturbations η and ϕ is

$$\left.\left(u_r^0 + \eta\frac{\partial u_r^0}{\partial r} + \frac{\partial\phi}{\partial r}\right)\right|_{R_{\text{in}}} = \left.\left(\frac{dR_{\text{in}}}{dt} + \frac{\partial\eta}{\partial t} + \Omega_{\text{in}}\frac{\partial\eta}{\partial\theta}\right)\right|_{R_{\text{in}}}, \tag{19}$$

where now all quantities are evaluated on the unperturbed surface R_{in}. Eq (19) converges to the kinematic boundary condition of Velikovich & Schmit (2015) for a non-rotating imploding liner when taking Ω_{in}=0. Using ansatz

$$\eta(\theta,t)=\eta_a(t)e^{im\theta},$$

from Eq. (19) we obtain:

$$-\frac{mB}{R_{\text{in}}^{m+1}}=\frac{d\,\eta_a}{dt}+im\Omega_{\text{in}}\,\eta_a+\frac{1}{R_{\text{in}}}\frac{dR_{\text{in}}}{dt}\,\eta_a. \tag{20}$$

Finally, pressure and surface perturbations are related by the dynamic boundary condition (Mikaelian 2005, Velikovich & Schmit 2015), implying that the full perturbed pressure is continuous across the perturbed surface:

$$\left(p^0+p'\right)\Big|_R=\left(p^0_{\text{in}}+p'_{\text{in}}\right)\Big|_R, \tag{21}$$

where the left side of equation corresponds to the liner fluid pressure and the right side corresponds to the gas pressure inside cavity. Taylor expansion of Eq. (21) up to linear terms in perturbations is

$$\left(p^0+\eta\frac{\partial p^0}{\partial r}+p'\right)\Bigg|_{R_{\text{in}}}=\left(p^0_{\text{in}}+\eta\frac{\partial p^0_{\text{in}}}{\partial r}+p'_{\text{in}}\right)\Bigg|_{R_{\text{in}}}, \tag{22}$$

Note that unperturbed pressures also satisfy dynamic boundary condition, i.e., $p^0(R_{\text{in}})=p^0{}_{\text{in}}(R_{\text{in}})$. Besides, we assume that gas in cavity is a passive medium which quickly equalizes the pressure inside an available volume. Therefore, $p^0{}_{\text{in}}$ is uniform in space ($\partial p^0{}_{\text{in}}/\partial r=0$) and $p'_{\text{in}}=0$ in linear approximation. Then Eq. (22) leads to

$$p'(R_{\text{in}})=-\eta\left(\frac{\partial p^0}{\partial r}\right)\Bigg|_{R_{\text{in}}}. \tag{23}$$

The gradient of unperturbed pressure can be found from equation of liner motion:

$$\frac{R_{\text{in}}}{r}\frac{d^2R_{\text{in}}}{dt^2}+\frac{1}{r}\left(\frac{dR_{\text{in}}}{dt}\right)^2-\frac{R_{\text{in}}^2}{r^3}\left(\frac{dR_{\text{in}}}{dt}\right)^2-\Omega^2 r+\frac{1}{\rho}\frac{\partial p^0}{\partial r}=0. \tag{24}$$

At $r=R_{\text{in}}$ this gives:

$$\left(\frac{\partial p^0}{\partial r}\right)\Bigg|_{R_{\text{in}}}=\rho\left(\Omega^2_{\text{in}}R_{\text{in}}-\frac{d^2R_{\text{in}}}{dt^2}\right),$$

and so

$$p'(R_{\text{in}})=\rho\left(\frac{d^2R_{\text{in}}}{dt^2}-\Omega^2_{\text{in}}R_{\text{in}}\right)\eta_a e^{im\theta}. \tag{25}$$

Eqs. (17), (20) and (25) constitute a closed system. Excluding $p'(R_{\text{in}})$ and B from them, we obtain the new Bell-type equation for the surface perturbation η_a:

$$\frac{d^2\eta_a}{dt^2}+2\frac{d\eta_a}{dt}\left(\frac{1}{R_{\text{in}}}\frac{dR_{\text{in}}}{dt}+im\Omega_{\text{in}}+i\Omega_\infty\right)+\eta_a\left[\frac{(1-m)}{R_{\text{in}}}\frac{d^2R_{\text{in}}}{dt^2}+(m-m^2)\Omega_{\text{in}}^2+2i\Omega_\infty\left(\frac{1}{R_{\text{in}}}\frac{dR_{\text{in}}}{dt}+im\Omega_{\text{in}}\right)\right]=0. \quad (26)$$

This equation converges to the known Bell stability equation for a non-rotating liner when taking $\Omega_\infty=\Omega_0=0$ (see, for example, Eq. (1b) in Mikaelian 2005). In this study Eq. (26) with the initial conditions $\eta_a(0)=\eta_{a0}$ and $d\eta_a/dt(0)=0$ is solved numerically using a 4th order Runge-Kutta scheme to obtain a complex solution for η_a. In order to follow the initial maximum and minimum points (spikes and bubbles) of the surface perturbation as the liner implodes, the corresponding polar angle $\theta(t)$ should be determined from the implosion trajectory and angular velocity. As first approximation, it is assumed that perturbation rotates with the base flow, i.e. the difference between angular velocity of perturbation minima/maxima and that of unperturbed liner is negligible. Then corresponding angle can be calculated as

$$\theta(t)=\theta(0)+\int_0^t\Omega_{\text{in}}(t')dt', \quad (27)$$

and the real evolution of perturbation maxima/minima is

$$\eta_{real}=\Re\left(\eta_a(t)e^{im\theta(t)}\right). \quad (28)$$

This evolution of perturbation maxima/minima is compared with full CFD simulations in Section 3.

Eq. (26) can be simplified if we account for the phase shift of the perturbation:

$$\eta_a=\bar{\eta}_a\exp\left(-im\int_0^t\Omega_{\text{in}}(t')dt'-i\Omega_\infty t\right),$$

then

$$\frac{d^2\bar{\eta}_a}{dt^2}+2\frac{d\bar{\eta}_a}{dt}\frac{1}{R_{\text{in}}}\frac{dR_{\text{in}}}{dt}+\bar{\eta}_a\left(\frac{(1-m)}{R_{\text{in}}}\frac{d^2R_{\text{in}}}{dt^2}+m\Omega_{\text{in}}^2+\Omega_\infty^2\right)=0. \quad (29)$$

Eq. (29) is similar in form to Eq. (2.20) from Huneault et al. (2019), the only difference is the presence of the term Ω^2_∞ in Eq. (29). We claim that our Eq. (29) can be applied to a liner with a general profile of angular momentum given by Eqs. (13), (14), whereas Eq. (2.20) from Huneault et al. (2019) only applies to a case of potential vortex, when L is constant in both radius and time (although analysis in that paper is done assuming initial solid body rotation with $L=\Omega_0 r^2$).

Eq. (29) can be futher simplified by introducing function $h(t)$, such that:

$$\bar{\eta}_a=h(t)\frac{R_{\text{in}}(0)}{R_{\text{in}}(t)}.$$

Then Eq. (29) becomes:

$$\frac{d^2h}{dt^2}+h\left(-\frac{m}{R_{\text{in}}}\frac{d^2R_{\text{in}}}{dt^2}+m\Omega_{\text{in}}^2+\Omega_\infty^2\right)=0. \tag{30}$$

For convenience, we give the relation of function $h(t)$ with full surface perturbation η:

$$\eta(\theta,t)=h(t)\frac{R_{\text{in}}(0)}{R_{\text{in}}(t)}\exp\left(im\theta-im\int_0^t\Omega_{\text{in}}(t')dt'-i\Omega_\infty t\right). \tag{31}$$

Eqs. (30), (31) describe the wave-like perturbation on the inner surface of the liner. The phase angular velocity of this wave (angular velocity of its spike) is

$$\Omega_{ph}(t)=\Omega_{\text{in}}(t)+\frac{\Omega_\infty}{m}. \tag{32}$$

Note that it is different from angular velocity of the inner surface of the liner $\Omega_{\text{in}}(t)$. The amplitude of this wave is growing as $R_{\text{in}}(0)/R_{\text{in}}(t)$ when liner is converging, as described by pre-factor in Eq. (31), and, in addition, it is oscillating or exponentially growing in time, depending on sign of the expression in brackets in Eq. (30). If

$$\frac{1}{R_{\text{in}}}\frac{d^2R_{\text{in}}}{dt^2}-\Omega_{\text{in}}^2-\frac{\Omega_\infty^2}{m}<0, \tag{33}$$

then the amplitude of perturbation is oscillating and the system is stable. In WKB approximation, the frequency of stable oscillations and growth rate of instability can be estimated by

$$\omega_{WKB}=\Im\sqrt{\frac{m}{R_{\text{in}}}\frac{d^2R_{\text{in}}}{dt^2}-m\Omega_{\text{in}}^2-\Omega_\infty^2}, \tag{34}$$

$$\gamma_{WKB}=\Re\sqrt{\frac{m}{R_{\text{in}}}\frac{d^2R_{\text{in}}}{dt^2}-m\Omega_{\text{in}}^2-\Omega_\infty^2}. \tag{35}$$

Presented analysis can be potentially extended to the case of a thin liner or for a number of cylindrical shells as part of a future work.

2.2.2 The WKB approximation

The perturbation on the liner outer surface is taken as zero as it is assumed to be pushed by a ring of pistons (Turchi et al. 1977). The perturbation motion is taken as governed by potential flow, as in the analysis presented in section 2.2.1 (Epstein 2004, Mikaelian 2005, Velikovich & Schmit 2015). As it has been shown in section 2.2.1, for the initially rotating liner angular momentum has to be of a certain form to ensure potentiality of the flow. In this WKB analysis we assume that the initial liner rotation corresponds to a potential vortex, i.e.,

$$L(r,t)=\Omega_0 R_{\text{in}}^2(0)$$

Therefore, for the potential velocity perturbation:

$$\vec{u}\,' = \nabla \phi, \quad \nabla^2 \phi = 0 \quad . \tag{36}$$

The general solution to the Laplace equation in polar coordinates is:

$$\phi = \left[A r^m + B r^{-m} \right] e^{i(m\theta + \omega t)}, \quad m > 0 \quad , \tag{37}$$

where the WKB approximation is in the assumption of exponential time variation.

The kinematic boundary condition on the liner inner surface was already given in Eq. (19). On the outer surface of the liner we assume that the surface perturbation $\eta=0$ which yields the simple boundary condition of a zero perturbation radial velocity; $u'_r = 0$ at $r=R_{out}$. The dynamic boundary condition was given in Eq. (22). Similar to Eq. (16), the perturbation pressure p' can be found through the linearised Bernoulli equation (Velikovich & Schmit 2015), i.e., $-p'/\rho = \partial\phi/\partial t + \vec{u}^0 \cdot \nabla \phi$, with $\vec{u}^0$ being the unperturbed velocity vector, so;

$$p' = -A\rho \left[i\bar{\omega} + m u_r^0 / r \right] r^m - B\rho \left[i\bar{\omega} - m u_r^0 / r \right] r^{-m} \quad , \quad \bar{\omega} \equiv \omega + m\Omega \quad , \tag{38}$$

where A and B are the same as in Eq. (37). Note that Eq. (38) does not contain terms with Ω_∞ as in Eq. (16), since $\Omega_\infty=0$ in a case of potential vortex rotation.

In order to find the characteristic equation for ω we combine the expressions for the perturbation velocity in Eqs. (36) and (37), pressure in Eq. (38) and the boundary conditions in Eqs. (19) and (22) which leads to a set of two linear equations that is symbolically written as:

$$\begin{pmatrix} d_{11} & d_{12} \\ d_{21} & d_{22} \end{pmatrix} \begin{pmatrix} A \\ B \end{pmatrix} = 0 \quad . \tag{39}$$

Taking the determinant of the matrix D leads to the characteristic equation for ω, where

$$d_{11} = m R_{out}^{m-1} \ , \ d_{12} = -m R_{out}^{-(m+1)} \quad , \tag{40}$$

by requiring $u'_r=0$ at $r=R_{out}$.

Neglecting the effect of the inner gas disturbance (i.e. taking Atwood number $\mathcal{A}=1$) greatly simplifies the equations. Furthermore, it was found for the cases studied in Section 3 that it did not affect much the stability for the studied examples. It should be noted, that the inner gas effect on the liner's unperturbed motion discussed in Section 2.1, is still accounted. Taking $\partial p^0_{in}/\partial r=0$ and $p'_{in}=0$ in Eq. (22), leads to:

$$d_{21} = -\rho \left(i\bar{\omega} + m u_r^0 / R_{\text{in}} \right) \left[i\bar{\omega} - \frac{\partial u_r^0}{\partial r} \right] R_{\text{in}}^m + m \frac{\partial p^0}{\partial r} R_{\text{in}}^{m-1} \quad , \tag{41}$$

and

$$d_{22}=-\left\{\rho\left(i\overline{\omega}-mu_r^0/R_{\text{in}}\right)\left[i\overline{\omega}-\frac{\partial u_r^0}{\partial r}\right]R_{\text{in}}^{-m}+m\frac{\partial p^0}{\partial r}R_{\text{in}}^{-(m+1)}\right\} \quad . \tag{42}$$

At the turnaround $u^0_r=0$, $\partial u^0_r/\partial r=0$ and by Appendix A, one can show that in order to have a real ω the unperturbed pressure gradient $\partial p^0/\partial r$ has to be positive, and by the momentum equation (1) it means a negative effective centripetal acceleration, i.e. $a_t=d^2R_{in}/dt^2-(u^0_\theta)^2/R_{in}<0$. An explicit analytical limit of stability for the liner's trajectory during implosion is derived in Appendix A to show that $a_t<-(dR_{in}/dr)^2/R_{in}$ for stability during the implosion. For the sake of completeness, a WKB approximation accounting for the perturbations inside the inner rotating gas is detailed in Appendix B.

The WKB approach can also be implemented in the new Bell-type stability equation (26) when assuming $\eta_a=\hat{\eta}_a e^{i\omega t}$ and substituting it into Eq. (26) while taking $d\eta_a/dt\simeq i\omega\eta_a$, $d^2\eta_a/dt^2\simeq-\omega^2\eta_a$ and similarly for h if using Eq. (30). It leads to a quadratic equation for ω, where the coefficients of $(i\omega)^n$, n=0,1,2 are the terms corresponding to $d^n\eta_a/dt^n$ in Eq. (26) or d^nh/dt^n if Eq. (30) is used. In essence, the WKB approximation turns the differential equation into an algebraic equation and it is an exact method of solution only when the algebraic equation does not depend on time (i.e. constant coefficients). Since the WKB approximation in Eqs. (26) or (30) and (39) is applied at different stages of the derivation, the two methods will yield different equations for ω. For sufficiently large m and/or large compression ratios (when $\Omega_{in}>>\Omega_\infty$), we have $\Omega_{in}^2>>\Omega_\infty^2/m$ and the WKB approximation of Eq. (30) leads to a negative effective centripetal acceleration as a necessary condition for stability (see Eq. (33)), pointing to the stabilising effect of the rotation.

2.3 CFD methodology

Full numerical simulations of the Navier-Stokes equations have been performed for the selected test cases to compare against the results obtained with linear stability analysis. Simulations are carried out using 'compressibleInterFoam' solver, which is part of the open source C++ libraries of OpenFOAM. 'compressibleInterFoam' is a multiphase solver which uses second-order VOF (Volume of Fluid) phase-fraction-based interface-capturing approach and is suitable for modelling two compressible immiscible fluids. The choice of the compressible solver was due to the compressibility of the inner gas. This solver has been extensively validated by the authors for a similar kind of problems and has been found to provide consistently reliable results with respect to the interface dynamics (Suponitsky et al. 2014 & 2017). Others approaches as the discrete

Boltzmann modelling are also possible (Lin et al. 2017), but the current approach was found to be sufficient. The schemes are all based on Gauss integration, using the flux and the advected field being interpolated to the cell faces by one of a selection of schemes. Second order “Gauss linear” scheme has been used in this study. For the viscous terms second order “Gauss linear uncorrected” scheme has been utilised. Second order temporal accuracy was achieved using the Crank-Nicolson approach. For more details see in OpenFOAM manual (2019). No turbulence modelling was used because of the very short time scale of the liner’s implosion as compared to the viscous time scale as shown in Section 3.3.

A schematic of the numerical setup used to study the evolution of the surface perturbations during the implosion of the 2D cylindrical liquid liner is shown in Fig. 2. Computations are done on a segment rather than over an entire cylindrical domain in order to reduce computational cost. The size of the segment is based on the polar mode number m of the perturbation; thirty degrees segment is used to study the evolution of m=6 perturbation (the lowest mode number being considered numerically) and the ten degrees segment for the mode m=36 and 72 perturbations. Periodic boundary conditions are applied on the sides of the segment as shown on Fig. 2. In the CFD simulations a compression of a gas target by an imploding liquid liner of a certain initial thickness is simulated. Implosion of the liner is caused by a pressurised gas with a prescribed temporal profile pushing on the outer surface of the liner.

Problem of the liner’s inner surface stability investigated with such a numerical setup is very similar to that considered in previous sections, but there are also some differences that worth emphasising. Here pressurised gas is used to implode the liner, rather than an array of pistons as considered in the linear stability analysis. Pushing pressure is applied as a boundary condition at the outer boundary of the computational domain, position of which remains unchanged during the simulation (Eulerian approach). As a result, as liner moves inwards, a volume occupied by gas is formed in between outer surface of the liner (that has now moved inwards) and stationary boundary of the computational domain. As pushing gas is treated as a compressible fluid, there is no guarantee that the pressure acting on the outer surface of the liner is identical to that imposed at the boundary of the computational domain. For the cases considered in this study the variation in the pressure felt by the outer surface of the liner and that prescribed at the boundary is negligible, but it can be more severe depending on the choice of implosion trajectory and parameters of the liner. When using gas to implode the liner, there is also a potential for development of interface instabilities (Rayleigh-Taylor and Kelvin-Helmholtz) at the outer surface of the liner, as light non-rotating gas is pushing

onto heavy rotating liquid. To minimize those effects, a sufficiently thick liner with unperturbed outer surface perfectly aligned with mesh lines, has been simulated. For those conditions the liner remains nominally smooth during the entire implosion apart of very small (fraction of mm in size) short wave-length Kelvin-Helmholtz structures developing from a numerical noise late in the compression.

The second important difference is that the dynamics of the inner gas during the implosion is actually been simulated. Hence, one can not ensure a spatially uniform pressure of the inner gas during the compression, and degree of uniformity depends on implosion trajectory and speed of sound in the gas. Again, with parameters considered in this study, this seems to have a very little effect on the inner liner surface evolution. One should keep in mind, that in the case of the rotating liner, there is a potential for development of Kelvin-Helmholtz instability at the inner surface of the liner if there is a jump in azimuthal velocity between gas and liquid. To minimize this, a rotational motion has been also imposed on the inner gas as initial condition for the simulation (as described farther below). It is also worth mentioning, that as gas target is being compressed during the implosion, the density ratio of liquid to gas decreases, by that effectively reducing Atwood number. For the cases considered here, density ratio remains high throughout implosion, so effect of Atwood number is expected to remain small. However, for implosion trajectories attaining very high compression ratios and also when lighter liners compress heavier gases, effect of Atwood number may become significant. Finally, viscosity and surface tension have been included in CFD simulations, unless it is stated otherwise.

At the start of simulations a liquid liner of predefined thickness surrounds a gas target that is to be compressed during the implosion. Initial velocity field in the liquid and inner gas is either set to zero for the non-rotating liner or to rotating as a solid body with angular velocity of Ω_0, i.e. $u_\theta^0 = \Omega_0 r$. As explained above, initial rotation of the inner gas is set to delay development of Kelvin-Helmholtz instability at the inner surface of the liner. The liquid liner is assumed to be incompressible, such that the corresponding initial pressure field i is prescribed as: $p^0(r, t=0) = p_{in} + \rho\Omega_0^2\left(r^2 - R_{in}^2(t=0)\right)/2$. Time dependent pushing pressure $p_{out}(t)$ is applied to the outer boundary causing the liner to implode. Radial extension of the computational domain corresponds to the outer radius of the liner or extends slightly beyond (as in Fig. 2). In the latter case, the initial pressure inside this thin gas layer is equal to the pushing pressure at time zero, $p_{out}(t=0)$. It has been concluded that the presence or absence of the thin gas layer does not affect the

resulting implosion trajectory. Both gas target and pushing gas behave as an ideal gas with an adiabatic constant of γ=1.4.

Simulations have been run for both unperturbed and perturbed at different polar modes and amplitudes inner surface of the liner. Perturbation imposed on the inner surface is defined as:

$$\eta = R_{in}(0) + \eta_0 \cos(m\theta) \quad , \tag{43}$$

where η_0 is the initial perturbation amplitude and m is a polar mode number. Perturbed at m=6 and unperturbed inner surface are shown in Fig. 2. The initial perturbation wavelength is therefore $\lambda_0 = 2\pi R_{in}(0)/m$. All simulations have been performed for a liner with inner and outer radii equal to $R_{in}(0)$=0.2 m and $R_{out}(0)$=0.282 m. For the low mode number (m=6) perturbation simulations, the number of grid points in the radial direction is N_r=3350, where 3000 points are placed inside the initial gas target and 350 are across the initial thickness of the liquid liner. Hence, the grid spacing varies monotonically from $\Delta r = 2*10^{-4}$ m to $\Delta r = 3*10^{-4}$ m for $r<R_{in}(t=0)$ and similarly for $R_{in}(t=0)<r<R_{out}(t=0)$. One thousand grid points were used in the polar direction. For the higher perturbation modes m=36 and 72, the number of the grid points in the radial direction was increased to N_r=5400, with 5000 points inside the gas target and 400 across the liner, leading to twice the resolution in the radial direction as compared to the low m=6 perturbation case. Four hundreds and two hundreds grid points were used in the polar direction for the simulations of m=36 and m=72 perturbations. Such grid resolutions resolve the relatively small amplitude initial perturbations as relevant for linear stability.

In the current setup, a small central portion of the computational domain $r<5*10^{-3}$ m has been excluded to avoid extremely small grid cells near the centre. For the cases in this study, maximum attained radial contraction ratios up to 10, and the effect of excluding a central part of the domain was found to be negligible. One should also note, that for implosions with high maximum radial contraction ratios, the non-linear effects will start manifesting themselves at some stage during the implosion, as the liner's inner surface converges towards the centre causing the perturbation's wavelength to decrease.

3. Results

All computations were carried for a liner with initial radii of $R_{out}(0)$ = 0.282 m and $R_{in}(0)$=0.2 m. The liner was assumed to be composed of water with density of 1000 kg/m^3 surrounding air at room temperature and 1 bar pressure at t=0. Viscosity and surface tension coefficients typical for water and air were assumed for the CFD simulations, but as it will be seen these coefficients had small

effect on the liner motion and perturbation. A constant pushing outer pressure of $p_{out}(0) = 5$ bar was taken to implode non-rotating liner, this was increased according to Eq. (5) for the rotating liners in order to achieve the same trajectory as of the non-rotating liner. In the CFD, the liner was assumed to be surrounded by air as illustrated in Fig. 2, but $p_{out}(t)$ at the boundary was specified according to Eq. (5).

The rotating liners were assumed to rotate as solid body at t=0 and thus $\Omega_\infty=\Omega_0$, see section 2.1 for details. First, analysis of the unperturbed liner trajectory is presented, followed by a comparison of the perturbation time development between the CFD and the new Bell-type stability Eq. (26). Consideration is given for non-linear perturbation development as exhibited by the CFD results near the turnaround point as well as effects of viscosity and surface tension, and finally a comparison between the Bell-type stability equation results and the WKB approximation is discussed.

3.1 Unperturbed Motion of the Liner

The pushing pressure profiles of $p_{out}(t)$ required to yield the same trajectory motion as of the non-rotating liner are shown in Fig. 3 for $\Omega_0=30$ rad/s and 60 rad/s along with a constant pressure profile used for a non-rotating liner. As expected, the higher initial rotational speed of the liner becomes, a higher pushing pressure is required in order to achieve the same implosion trajectory of the non-rotating liner and counter-act the centrifugal force caused by the liner's rotation. In fact, it is seen from Fig. 3, that the peak pressure increases as a square of rotational velocity relative to the constant pushing pressure for the case of a non-rotating liner, as per Eq. (5). For the current set of parameters, the peak pushing pressure, occurring near the turn-around point, for the liner initially rotating at 60 rad/s is about ten times higher than for a non-rotating liner.

Numerical simulations have been run for the non-rotating and rotating at $\Omega_0=60$ rad/s liners with the corresponding pushing pressures shown in Fig. 3. Implosion trajectory obtained in those simulations together with that obtained from the 1D model given by Eq. (2), are shown in Fig. 4. One can see that the implosion trajectories obtained from the numerical simulations at different rotational speeds and adjusted pushing pressures are identical and are also in an excellent agreement with the trajectory obtained by the 1D model given by Eq. (2). Therefore, we have a numerical set-up proven to be capable of reproducing the same implosion trajectory at various rotational speeds. The results agree well with those obtained by Eqs. (2) and (5), that are also used in the linear stability analysis.

The radial compression ratio is up to about ten is shown in Fig. 4. This yields a maximum pressure of about 35 MPa at the turnaround point by Eq. (4). Such pressure is much smaller than the bulk modulus of water which is 2.15 GPa and compose the liner. Hence, the assumption of incompressible flow for the liquid liner is justified for the studied cases.

While implosion trajectories are the same at all rotational speeds due to the increase in $p_{out}(t)$ to counteract the centrifugal force acting on the implosion trajectory, the effective centripetal acceleration $a_t = d^2R_{in}/dt^2 - \Omega^2_{in}R_{in}$ experienced by the liner's inner surface depends on the rotation rate. Acceleration curves for the liners are shown in Fig. 5 which also include the WKB approximation stability limit of $a_t < -(dR_{in}/dt)^2/R_{in}$ that was derived in Appendix A. All liners initially show an effective centripetal acceleration a_t that is lower than the WKB stability limit and thus by that approximation they should show linear stability. However, towards the turnaround point both the non-rotating liner and the one with Ω_0=30 rad/s show a positive a_t and thus by the WKB approximation they should show linear instability. On the other hand, the fast rotating liner of Ω_0=60 rad/s shows an effective centripetal acceleration that is sufficiently negative to be lower than the WKB stability limit. Thus by that approximation, the liner should be linearly stable up to the turnaround point and show no exponential growth of perturbation as the WKB approximation assumes.

3.2 Perturbation time development

CFD simulations have been carried out for the non-rotating and rotating liners of Ω_0=30 rad/s and 60 rad/s with the inner surface perturbed at polar mode numbers *m*=6, 36 and 72. Before presenting and discussing the results it is important to re-iterate several points:

(i) A reasonable agreement between the results of CFD simulations and linear stability analysis can be expected only when the ratio between perturbation amplitude and wavelength is small, i.e. $\eta/\lambda << 1$.

(ii) Because of the liner's geometrical convergence, the perturbation wave length λ decreases during the implosion until reaching the turnaround point, since $\lambda(t) = 2\pi R_{in}(t)/m$. Therefore, even if the perturbation amplitude does not grow during the implosion, non-linear effects will manifest themselves sooner or later if high radial compression ratios are attained. For the implosion trajectory considered in Fig. 4, the maximum contraction ratio is around 10, therefore even without perturbation growth and for the initial perturbation amplitudes considered here, some non-linear effects are expected to appear near turnaround point and, in particular, at high polar mode numbers perturbations.

(iii) The WKB approximation assumes an exponential time growth or a sinusoidal time oscillation. This is not necessarily accurate. A more accurate solution is given by the Bell-type stability equation (26) that yields results that are also easier to compare to those obtained with CFD. Hence, in this section the Bell-type stability solution is compared with the CFD results. This stability equation assumes infinitely thick liner. The current liner starts with a thickness ratio of 0.4 as compared to the inner radius, and it grows during implosion. Furthermore, the effect of the liner finite thickness rapidly decreases with the polar mode number *m* because the perturbation decays as $1/r^m$ away from the inner surface, see Eq. (8). Therefore, at least at high polar modes, the assumption of the infinitely thick liner should hold well.

To extract the perturbation evolution from the CFD simulations, the locations of minimum (spike) and maximum (bubble) of the initial perturbations have been tracked during the simulations by the VOF value equal to 0.5. In order to obtain a perturbation amplitude during the implosion the corresponding position of the unperturbed liner inner surface has been subtracted. For the non-rotating liners, the polar angle θ initially corresponding to minimum and maximum of the perturbation, remains unchanged during the implosion. For the rotating liner, a specific point placed on the inner surface rotates during the implosion. The polar angle $\theta(t)$ of a particular point initially placed at polar angle $\theta(0)$ is given by Eq. (27). That equation assumes the angular velocity of the perturbed interface is the same of the unperturbed one. As the ratio between perturbation amplitude and unperturbed radius $\eta(t)/R_{in}(t)$ increases (mainly due to the decrease in $R_{in}(t)$ as the liner converges), the angular velocity on the perturbed surface starts to deviate from its unperturbed value due to the conservation of angular momentum resulting in transforming the initially `cosine' shaped perturbation towards the `breaking wave' shape as will be seen in the next sub-section. This study is focused on the linear stability process and hence, the unperturbed rotational speed Ω_{in} is used in Eq. (27).

'Spike' is referred to the evolution of a point initially extending into the gas, whereas 'bubble' is referred to the evolution of a point initially extending into the liquid as illustrated in Fig. 2. Depending on the number of phase inversions a 'spike' can become a 'bubble' and vice-versa, but the names in this paper are determined by the positions at the start of the simulation. For the small amplitude perturbations, evolution of 'spike' and 'bubble' is the same, but when non-linear effects start to play a role, the differences are expected to develop, and one of them may correlate better with the linear solution than the other.

Keeping this in mind, the time-developments of the perturbation amplitude for m=6, 36, 72 and Ω_0 = 0, 60 rad/s are given in Figs. 6 and 7, where for the linear stability the real part of $\eta(t)$ (see Eq. (28)) is plotted. As expected, there is a very good agreement between the Bell type linear stability (Eq. 26) and CFD results for early times in all cases. The non-rotating liners also show amplitude growth, particularly for *m*=6 near the turnaround point. This is expected due to the positive effective centripetal acceleration a_t shown in Fig. 5a, leading to Rayleigh-Taylor rapid growth. The agreement between the linear stability and CFD deteriorates at later times, particularly around the turnaround point. We believe this is due to non-linear effects that particularly manifest themselves at the high *m*=72 as explained earlier. Similar observation was experimentally made by Huneault at al. (2019). Increasing the polar mode *m* also enhances the oscillatory behaviour of η, yielding a Bell-Plesset behaviour. This increase in oscillatory behaviour can be explained examining the expression for perturbations growth rates obtained with WKB analysis of Bell-type equation, see Eqs. (34) and (35) for the details. From those equations one can see that oscillation frequency is proportional to square root of polar mode m for non-rotating liners.

Increasing the rotational speed to Ω_0=60 rad/s has damped the amplitude growth for *m*=6 perturbation near the turnaround point (t~7.2 ms) as can be seen from Fig. 7a and is in agreement with the negative a_t seen in Fig. 5c. In reality, non-linear effects near the turnaround point can saturate and even damp the perturbation amplitude growth as seen in Fig. 7c for *m*=72. One can also see from Figs. 6 and 7 that increase in rotation increases frequency of oscillatory behaviour for the perturbation at the same polar mode. The perturbation amplitude, however, is not affected significantly during the acceleration stage of the liner implosion.

3.3 Consideration of non-linear evolution of the inner surface near the turnaround point.

Although the analytical analysis presented here focuses on the linear stability process, the CFD results also provide valuable insight into the non-linear process that can dominate the perturbation development at later times and particularly for high polar modes. Hence for completeness, a brief description of this process is given here. It should be noted that since the CFD only considered an annular segement of the liner, the non-linear interaction between the polar modes was limited.

The time evolutions of the inner surface are shown in Fig. 8 for the CFD results corresponding to *m*=6 and Ω_0=0, 30 and 60 rad/s. The perturbation develops into a bubble and spike and remains symmetric for Ω_0=0 rad/s keeping its initial form as expressed in Eq. (27). The rotational speed causes a deformation in the perturbation, breaking the symmetry and leading to a breaking wave as

particularly seen in Fig. 8d for Ω_0=30 rad/s. It also leads to a breaking of a small part of the liner from the rest. On the other hand, the liner of Ω_0=60 rad/s shows an intact liner but with wavy surface at t=7.4 ms. Shape of breaking wave structures developed in case of rotating liners, seem to resemble Kelvin-Helmholtz rollers. We tend to believe that those structures develop because of different rotational velocity at different radii, rather than being a product of Kelvin-Helmholtz instability. As radius decreases, rotational velocity increases, this causes crest of perturbation at the smaller radius to experience higher rotational velocity, whereas the gas penetrating into the liner experiences the slower rotational velocity. For a lower polar mode m=6 perturbation evolution, there is only one phase inversion during the compression being considered, therefore, from about 3.5 ms, the same portion of liquid/gas experiences higher or slower azimuthal velocity which over a time results in inclination of the structure.

The time evolutions of the inner surface for m=72 are shown in Fig. 9. The case of Ω_0=0 rad/s shows a clear development of bubbles penetrating the liner, breaking the integrity of the liner's inner surface. Increasing the rotational speed to Ω_0=60 rad/s significantly damps the surface perturbation as already seen by Fig. 7c for the amplitude's time-development, leading to an inner surface that is intact for this mode. This finding qualitatively agrees with the non-linear RT stability analysis of Tao et al. (2013), who pointed to the saturation effect of the rotation in the non-linear stage of the perturbation development. However, it should be noted that the acceleration or deceleration of the interface surface was due to the disturbance in Tao et al's (2013) analysis and not due to any imploding motion as in this study.

Removing the surface tension from the CFD simulation as it was done for the liner on the right-hand side of Fig. 9, shows no noticeable difference with the simulation that accounts for the surface tension seen at the centre of Fig. 9. Hence, the damping of the perturbation is due to non-linear effects and not surface tension. This can be re-enforced by the following scaling analysis. First, the viscous time scale is l^2/υ , where l is the shortest relevant length scale and in this case is taken as the liner's inner surface perturbation wave length, i.e. $l=2\pi R_{\text{in}}/m\simeq 0.22\ cm$ for m= 72 near the turnaround. The water's kinematic viscosity coefficient is $\upsilon=0.0114\ cm^2/s$, yielding a viscous time scale of 4 s which is much longer than the implosion's time scale of 8 ms seen in Fig 4. More specific estimates for particular cases as the Taylor and Oseen vortices confirm a viscous time scale between 4 s to 1 s (Panton 2005). The ratio of the initial amplitude and wave length of the perturbation for m=72 polar mode, is about 0.0175 for the parameters being considered. With maximum radial compression of about 10, this ratio will increase 10 times to about 0.175 even if

perturbation does not grow as liner implodes. The ratio of 0.175 between amplitude and wave length of perturbation is sufficiently large for nonlinear effects to manifest themselves.

The scaling of the surface tension effect can be estimated using the "classical RTI" as suggested by Turchi (2017b) for imploding liners, i.e. neglecting the term $\eta \partial u_r^0 / \partial r$ and rotation in Eq. (19), the liner's radius for a high polar mode and using the WKB approach. Adding the effect of the surface tension leads to (Lamb 1945);

$$\omega^2 = \frac{\rho_{\text{in}} - \rho}{\rho_{\text{in}} + \rho} a_t k + \frac{\gamma k^3}{\rho_{\text{in}} + \rho} \quad . \tag{44}$$

The surface tension coefficient is $\gamma = 0.0714 \ N/m$ for water-air interface, the inner surface wave number is $k = m/R_{in}$ and the effective centripetal acceleration is $a_t \sim 10^4$ m/s^2 or higher by Fig. 5. This yields a magnitude of 10^{-5} for the second term on the right hand side of Eq. (44) as compared to the first term on the right hand side, further justifying the omission of the surface tension from the current stability analysis.

It is finally worth mentioning, that despite imposing initial rotation in the inner gas, development of Kelvin-Helmholtz instability has been observed late into the compression. For the low polar mode perturbation m=6, small scale Kelvin-Helmholtz structures have developed on top of a primary low mode perturbation, whereas for the high mode m=72 perturbation, zooming into the interface region reveals presence of short wave-length Kelvin-Helmholtz structures along the entire interface, making interface look more like a thin foamy region, rather than a sharp line. Zoom into interface region near the turnaround point is shown in Fig. 10, where the left and right parts of the figure correspond to low and high polar mode perturbation, respectively. It should be noted, however, that the size of those structures is very small compared to the radius of the liner's inner surface, e.g. near the turnaround point, radius of the inner surface is just under 3 cm, while the radial extension of Kelvin-Helmholtz structures is about 1/3 of a millimeter (Fig. 10b).

3.4 The WKB approximation

The time development of the inner surface perturbation η according to the WKB approximation of Appendix A was compared to the exact solution of the Bell-type equation (26) and its WKB approximation. The comparison is shown in Fig. 11 for the liners of Ω_0=0 and 60 rad/s and m=6 and 72. In all cases there is a good agreement between all three solutions at early time stages except for m=72 and Ω_0=60 rad/s where the WKB approximation of the Bell-type equation (26) starts to deviate and show strong oscillations. It shows that the WKB approximation can be considered as an

accurate solution at early development of the perturbation and when there is no rapid change in the liner's unperturbed motion.

The WKB approximation of Eq. (A1) is more affected by the polar mode m than the initial rotational speed Ω_0, where it is re-iterated that for simplicity Ω_∞ was taken as zero for the derivation in Appendix A, i.e. the liner started from a vortex motion. This follows the argument of Turchi (2017) that the initial stage of rotation whether solid or vortex has a small effect on the stability towards the turnaround point. Nevertheless, comparing Fig. 11a with Fig. 11c shows damping for Ω_0=60 rad/s towards the turnaround point of t=7.3 ms, which agrees with the stability limit derived in Appendix A. On the other hand, the exact solution of Eq. (26) shows oscillatory growing amplitude towards the turnaround point as was already seen in Fig. 7c. CFD solution also showed an oscillatory motion for the perturbation, but with a decreasing amplitude towards the turnaround point due to non-linear effects. Hence, stability arguments based on linear theory should be applied with caution near the turnaround point. Nevertheless, in overall the exact solution of Eq. (26) agrees best with the CFD solution seen in Figs. 7 when also comparing the WKB approximations.

Adding the effect of the inner gas perturbations, using Appendix B WKB approximation that accounts for the deviation of the Atwood number $\mathcal{A}$ from one, did not change much the solution and only moderately deviated from the solution of Appendix A towards the turnaround point. This can be understood by the initial high density ratio of about 1000 between the liner's liquid and the inner gas which reduced to about 10 at the turnaround point. Hence, the mild change in the Atwood number during the liner's implosion caused expressions (B5) and (B6) to be similar to those which yielded solution (A5). Therefore, for radial contraction ratios of up to at least ten, the inner gas perturbations may be neglected in the linear stability analysis with a small effect on the solution, strengthening again the approach of the new Bell-type stability equation (26) for these kinds of contraction ratios.

4. Conclusions

New linear hydrodynamic stability theory was presented for the case of imploding rotating cylindrical liquid liner compressing an inner trapped gas. The study was divided into two parts; (i) unperturbed motion analysed using a 1D equation of motion and (ii) the time development of an inner surface perturbation. New Bell-type stability equation was derived for the case of infinitely thick rotating liner along with new WKB approximations for a finite and an infinitely thick rotating liners. CFD solution was used to compare with the two approaches. To pinpoint the effect of the

rotation, the pushing pressure on the rotating liner was increased in order to achieve the same trajectory of unperturbed motion as the non-rotating liner that was subject to a constant pushing pressure.

Excellent agreement was achieved between the CFD solution and the 1D solution of the unperturbed motion. Very good agreement was also achieved between the CFD solution and the perturbation growth according to the new Bell type stability equation, except when non-linear effects started to kick in near the turnaround point. Good to fair agreement was achieved between the Bell type solution and the WKB approximations, pointing to a need of caution when using that approximation. Effects of viscosity, surface tension and inner gas stability waves were found to be small for the liners studied here, reaching a contraction ratio of up to 10:1 in the liner's inner radius. This was justified by the CFD results and scaling analysis.

Hence the following conclusions can be made about the physical behaviour of the stability process:
1) During the initial accelerating stage of the liquid liner, perturbation undergoes slow oscillatory growth due to the convergence, i.e. Bell-Plesset effects. Rotation has an insignificant effect on the perturbation amplitude during this time for the liner's parameters and perturbations studied here.
2) During the decelerating stage of the liquid liner, exponential perturbation growth due to the classical Rayleigh-Taylor instability can be suppressed by a sufficiently high rotation of the liner. Linear stability analysis predicts that slow oscillatory growth remains even when the exponentially growing RT instability is suppressed. Results of CFD simulations demonstrate that this oscillatory growth is damped when ratio of amplitude to wavelength of perturbation becomes sufficiently high for non-linear effects become significant.
3) While operating in the range of the suppressed exponential growth during the decelerating stage, a 'smooth' collapse of the initially unperturbed liner can be achieved. As a result, a non-linear evolution of the initially perturbed liner can be studied in the a 'clean' numerical environment, i.e. without contamination by high frequency sporadicly growing perturbations. Numerical simulations have shown that in the case of the initially perturbed liner in the regime of suppressed RT instability, the inner surface of the liner does not disintegrate despite presence of evolving perturbation.

Acknowledgement:
This research was supported by General Fusion. We would like to thank the anonymous referees and the editor Dr. Stefan Llewellyn Smith for their valuable comments on the manuscript.

References:

Avital E 1995, Asymmetric instability of a viscid capillary jet in inviscid media, *Phys Fluids* **7,** 1162-1164

Avital EJ**,** Salvatore E, Munjiza A, Suponitsky V, Plant D, Laberge M 2017, Flow design and simulation of a gas compression system for hydrogen fusion energy production, *Fluid Dyn Res* **49,** 045504

Barcilon A, Book DL and Cooper AL 1974, Hydrodynamic stability of a rotating liner, *Phys Fluids* **17,** 1707-1718

Book DL and Winsor NK 1974, Rotational stabilization of a metallic liner, *Phys Fluids* **17,** 662-663

Book DL and Turchi PJ 1979, Dynamics of rotationally stabilized implosions of compressible cylindrical liquid shells, *Phys Fluids* **22** (1979) 68-78

Drazin OG and Reid WH 2004, *Hydrodynamic Stability 2nd Ed*, Cambridge Univ Press, Cambridge, 2004

Epstein R 2004, On the Bell-Plesset effects: The effects of uniform compression and geometrical convergence on the classical Rayleigh-Taylor instability, *Physics of Plasmas* **11**(11), 5114-5124

Huneault J, Plant D and Higgens AJ 2019, Rotational stabilisation of the Rayleigh-Taylor instability at the inner surface of an imploding liquid shell, *J Fluid Mech* **873**, 531-567

Kull HJ 1991, Theory of the Rayleigh-Taylor instability, *Physics Reports* **206,** 197-325

Lamb, H 1945 *Hydrodynamics*, Dover Pub, New York

Lin C, Xu A Zhang G, Luo KH and Li Y 2017, Discrete Boltzmann modeling of Rayleigh-Taylor instability in two-component compressible flows, *Phys Rev E* **96**, 053305

Mikaelian KO 2005, Rayleigh-Taylor and Richtmyer-Meshkov instabilities and mixing in stratified cylindrical shells, *Physics of Fluids* **17,** 094105

Open Foam manual 2019 https://www.openfoam.com/documentation/ (accessed 21 May 2019)

Panton RL 2005, *Incompressible Flow 3rd Ed*, Wiley, New Jersey

Suponitsky V, Froese A and Barsky S 2014, Richtmyer-Meshkov instability of a liquid-gas interface driven by a cylindrical imploding pressure wave, *Computers and Fluids* **89**, 1-19.

Suponitsky V, Avital E, Plant D and Munjiza A 2017, Pressure Wave in Liquid Generated by Pneumatic Pistons and Its Interaction with a Free Surface, I*nt J Applied Mech* **9,** 1750037

Suponitsky V, Khalzov IV, Zimmermann J and Plant D 2018, Concept of rapidly decelerating turbine-like apparatus to form an imploding liquid liner, Proc 26th Annual Conf Comp Soc Canada, Winnipeg, Manitoda, Canada

Tao JJ, He XT and Ye WH 2013, Nonlinear Rayleigh-Taylor instability of rotating inviscid fluids, *Phys Rev E* **87**, 013001

Turchi PJ, Cooper AL, Ford R and Jenkins DJ 1976, Rotational stabilization of an imploding liquid cylinder, *Phys Rev Letts* **36,** 1546-1548

Turchi PJ, Jenkins DJ, Ford RD and Cooper AL 1977, *Rotational stabilization of the inner surface of a piston-driven imploding liner*, USERDA E(49-26)-1009 ED-03-0

Turchi PI 2017a, Stabilized liner compressor for low-cost controlled fusion at megagauss field levels, *IEEE Trans Plasma Sci* **45,** 2800-2809

Turchi PJ 2017b, Imploding liner compression of plasma: Concepts and issues, *IEEE Trans Plasma Sci* **45,** 2800-2809

Vadivukkarasan M and Panchagnula M 2019, Destabilization characteristics of three dimensional Rayleigh-Taylor mechanism on a cylindrical interface, *Meccanica*, DOI 10.1007/s11012-019-01086-0

Velikovich AL and Schmit PF 2015, Bell-Plesset effects in Rayleigh-Taylor instability of finite-thickness spherical and cylindrical shells, *Physics of Plasmas* **22,** 122711

Wang LL, Xu J, Wang Y, Wei G, Lin C and Zhu H 2018, Reduction of internal-solitary-wave-induced forces on a circular cylinder with a splitter plate, *J Fluid Struct* **83**, 119-132

List of Figures:

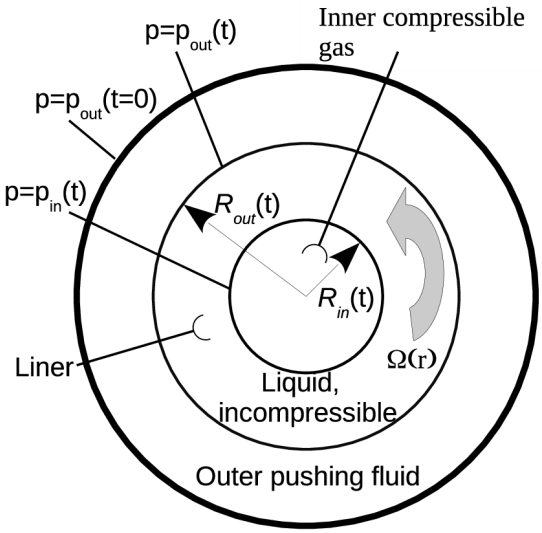

Figure 1: Schematic description of the cylindrical liner cross-section

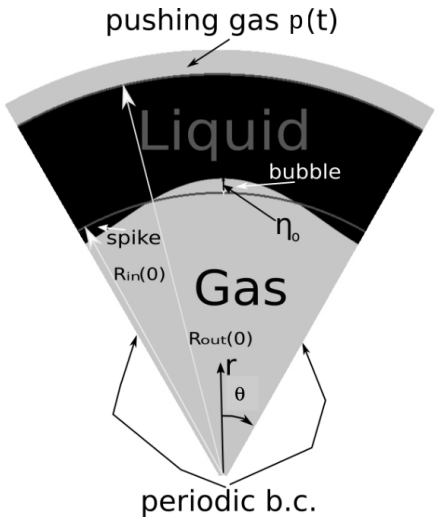

Figure 2: A schematic of the numerical setup for the CFD simulation

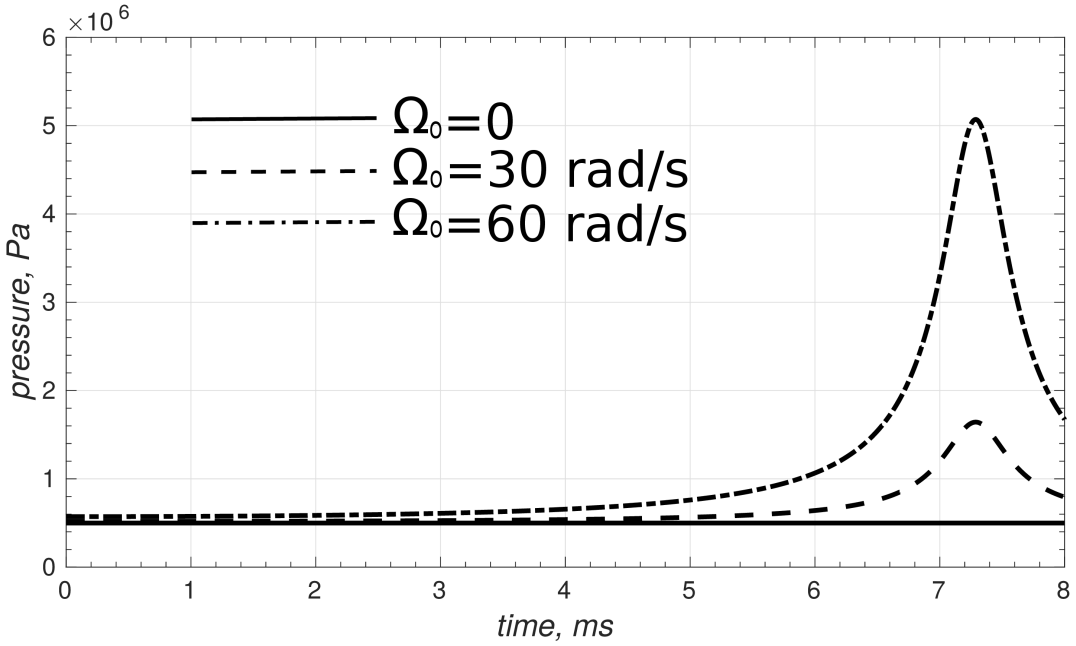

Figure 3: Pushing pressure $p_{out}(t)$ profiles as required by Eq. (5) in order to overcome the centrifugal force and achieve the same trajectory as of the non-rotating liner that is subjected to a constant $p_{out}(t)$=5 bars.

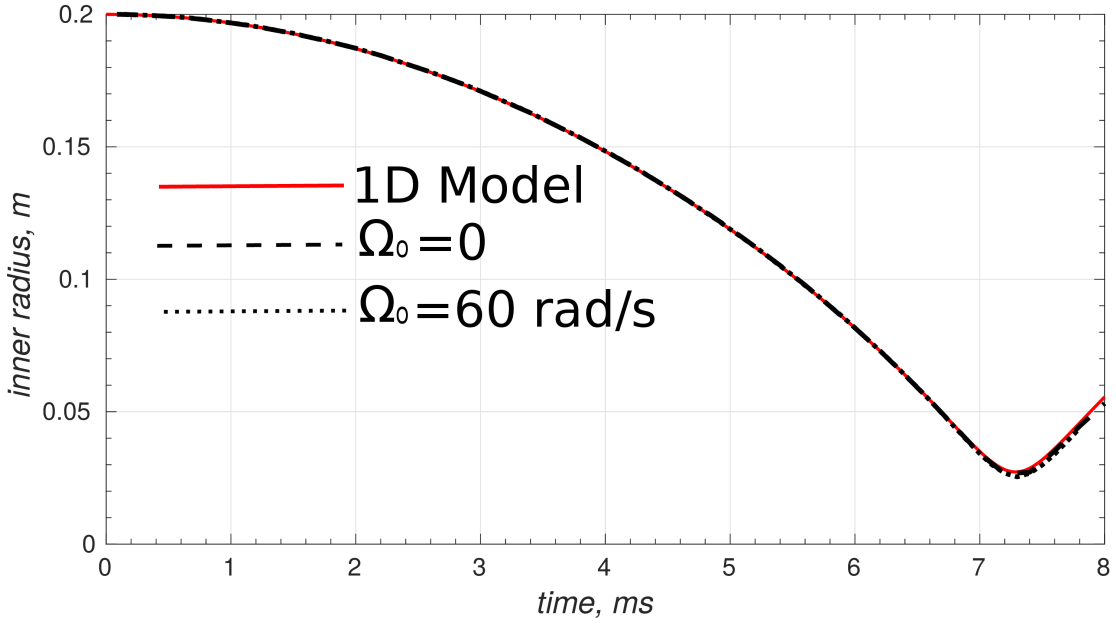

Figure 4: The implosion trajectories as calculated by the 1D motion equation (2) which is noted as 1D model and the CFD simulations of unperturbed liners for Ω_0=0 and 60 rad/s that were subjected to the pushing pressure $p_{out}(t)$ plotted in Fig. 3.

(a)

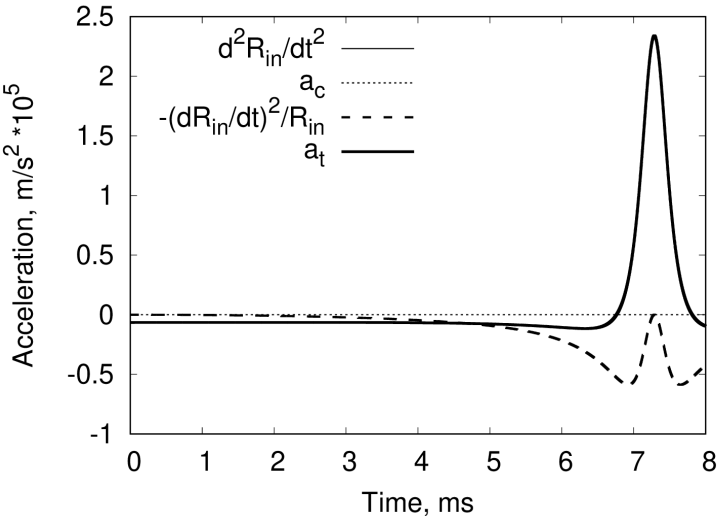

(b)

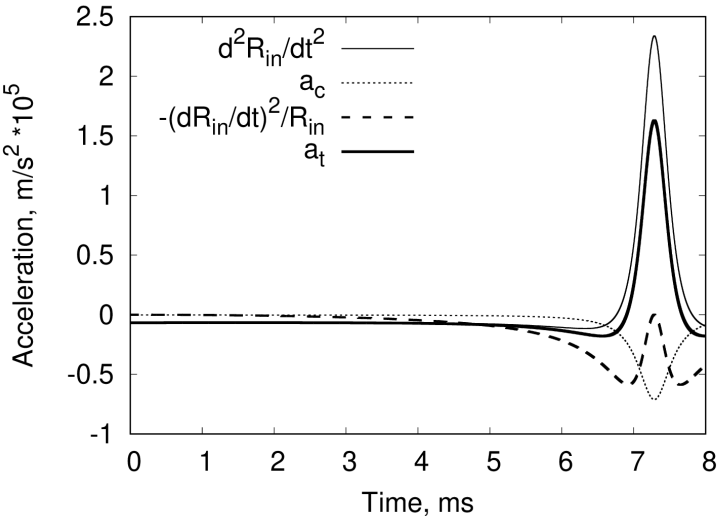

(c)

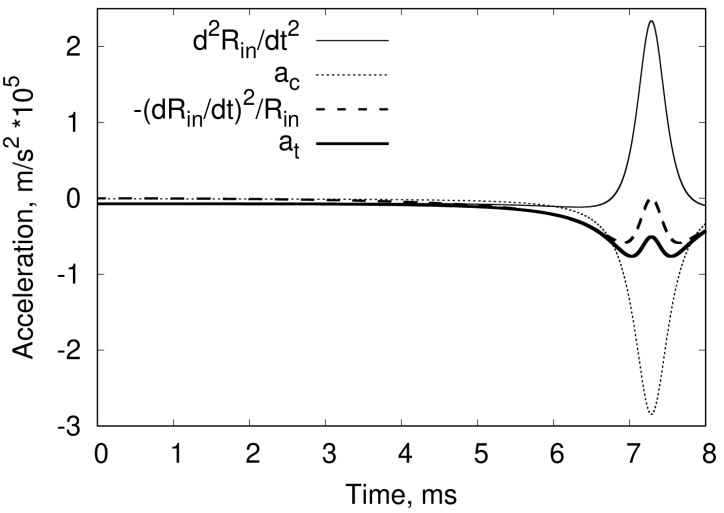

1 Figure 5: Acceleration time histories that were calculated for the implosion trajectory shown in Fig.
2 4 and for (a) Ω_0=0 rad/s, (b) Ω_0=30 rad/s and (c) Ω_0=60 rad/s.

(a)

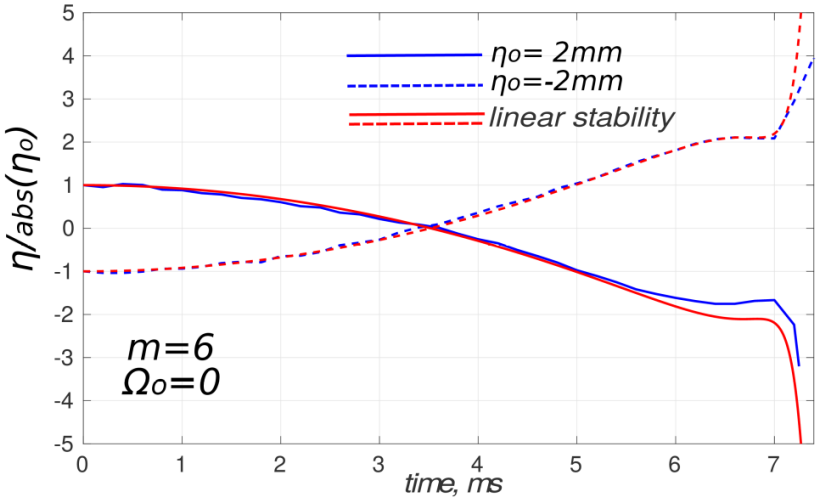

(b)

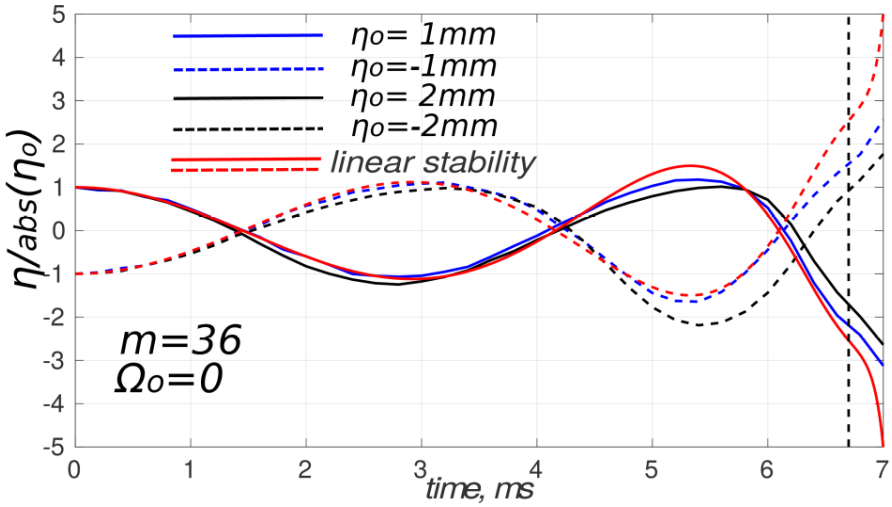

(c)

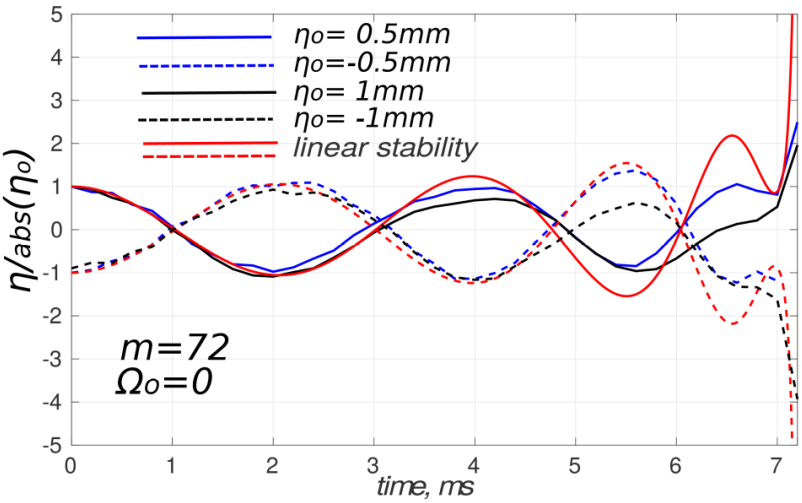

1 Figure 6: Time developments of perturbation amplitude normalised by its initial absolute value as
2 predicted by the CFD computations and the Bell-type linear stability Eq. (26) for the non-rotating
3 liners and polar mode number of (a) m=6, (b) m=36 and (c) m=72.

(a)

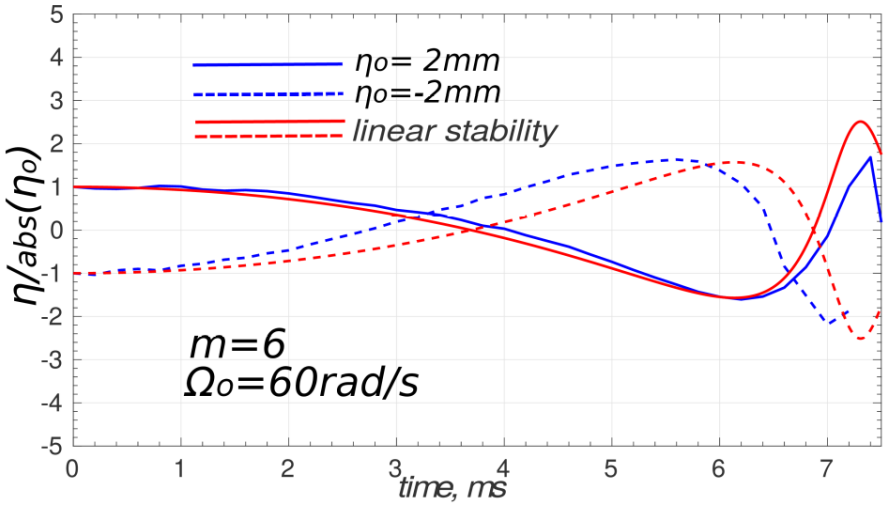

(b)

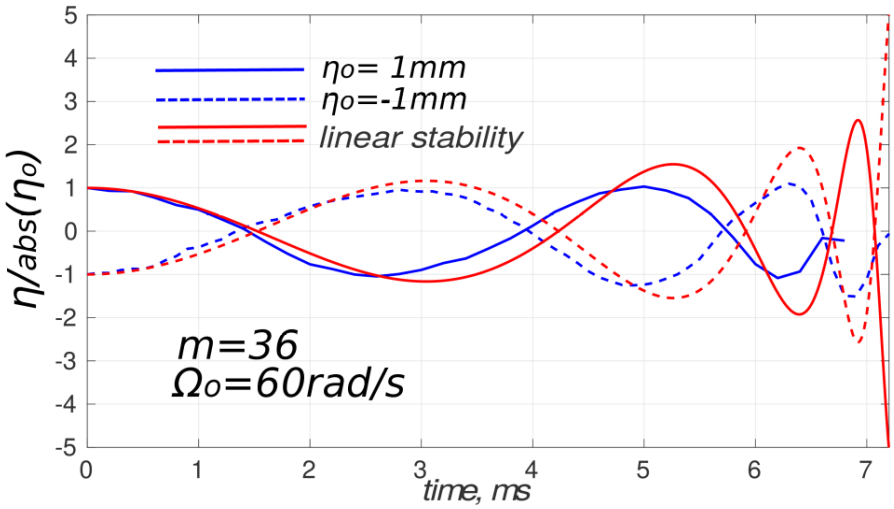

(c)

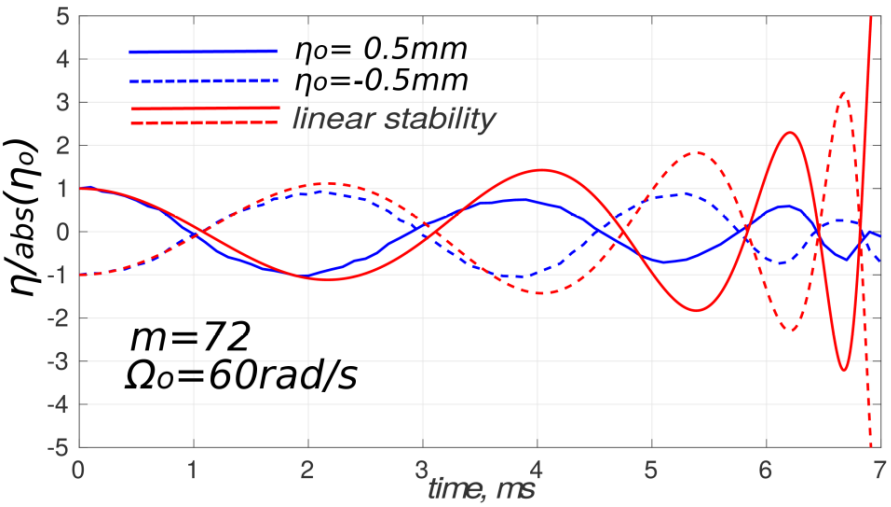

Figure 7: Time developments of perturbation amplitude normalised by its initial absolute value as predicted by the CFD computations and the Bell-type linear stability Eq. (26) for the rotating liners of Ω_0=60 rad/s and polar mode number of (a) m=6, (b) m=36 and (c) m=72.

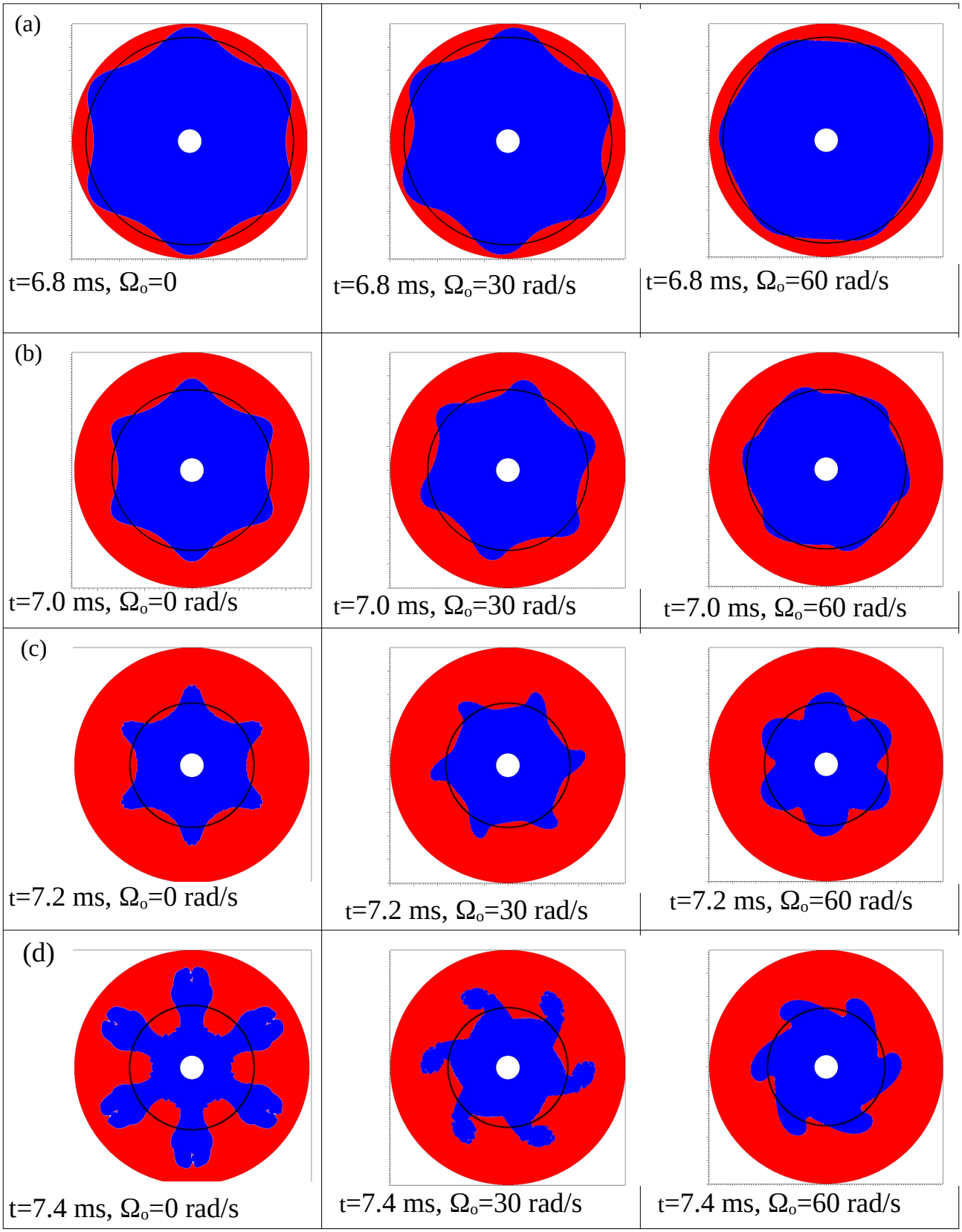

Figure 8: Instantaneous contours of the liner's inner surface around the turnaround point for polar mode m=6 as produced from the CFD simulations. Radial extension of the enlarged central portion of the domain is 5 cm. Red (outer) – liquid liner, blue (inner) – gas target, black line – position of unperturbed interface.

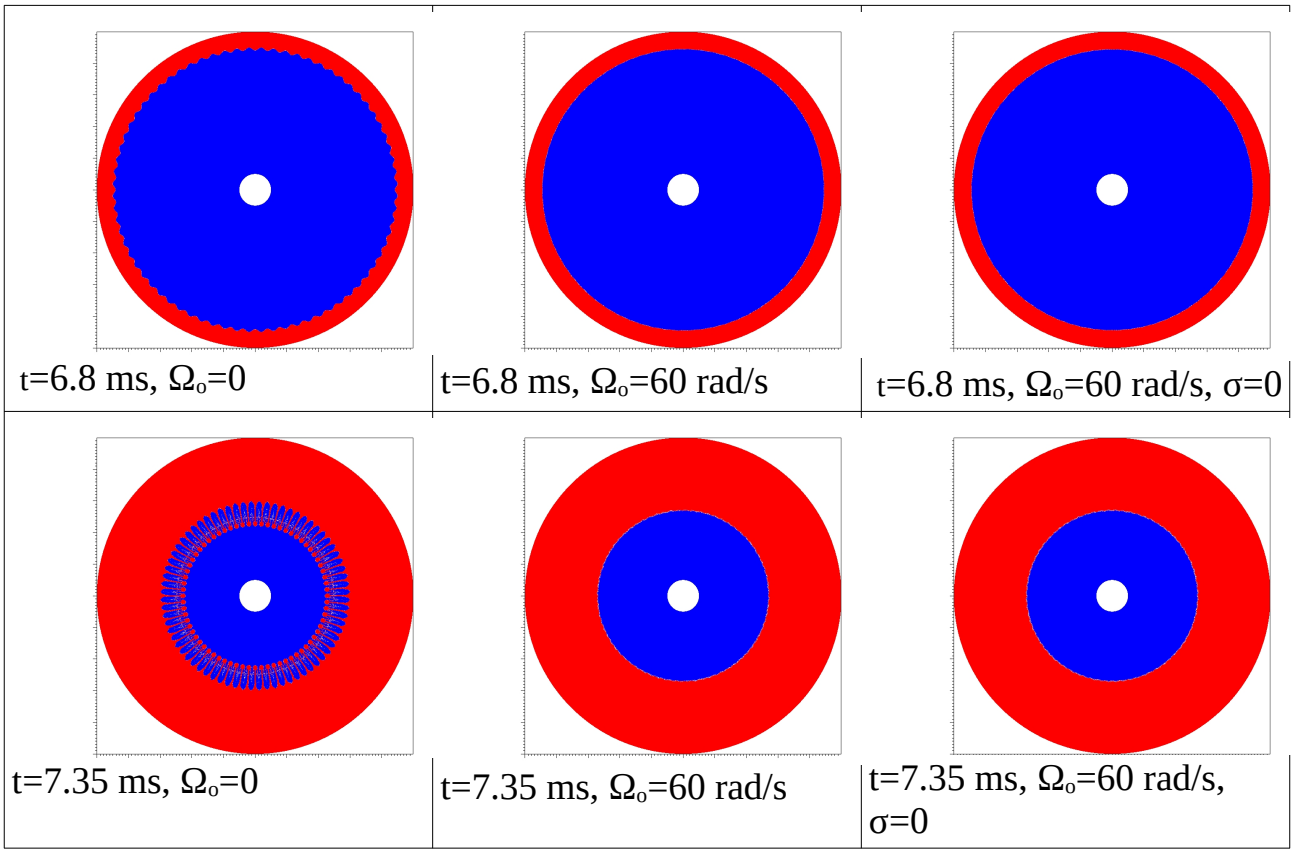

Figure 9: Instantaneous contours of the liner's inner surface around the turnaround point for polar mode m=72 as produced from CFD simulations, where the right- column liner simulation did not account for surface tension (σ=0) unlike the other two simulations. Radial extension of the enlarged central portion of the domain is 5 cm. Red (outer) – liquid liner, blue (inner) – gas target.

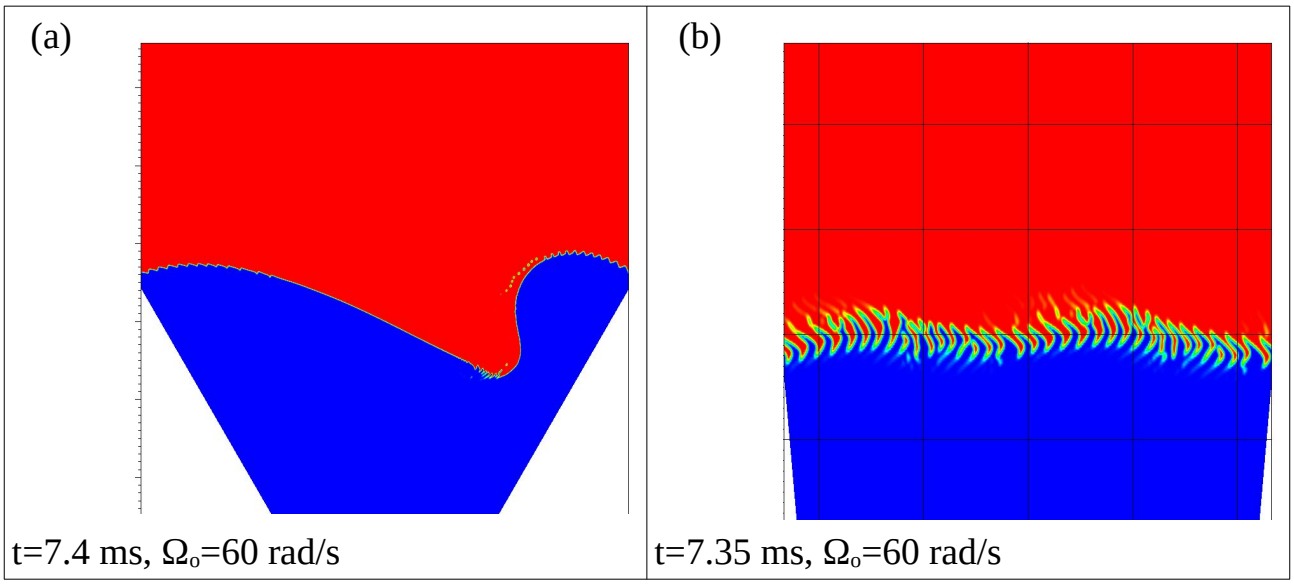

Figure 10: Zoom in on the interface for polar mode m=6 (a) and m=72 (b) for the results shown in Figs. 8 and 9. Scale (distance between major ticks on the grid) is 5 mm for m=6 plot and 1 mm for m=72 plot. Red (outer) – liquid liner, blue (inner) – gas target.

(a)

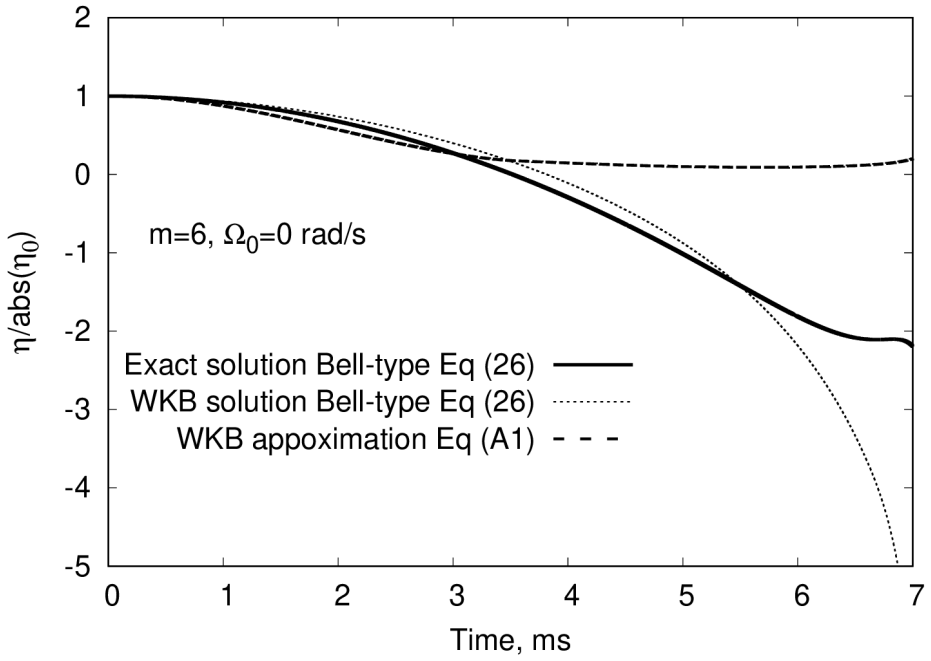
m=6, Ω0=0 rad/s
Exact solution Bell-type Eq (26)
WKB solution Bell-type Eq (26)
WKB appoximation Eq (A1)
η/abs(η0)
Time, ms

(b)

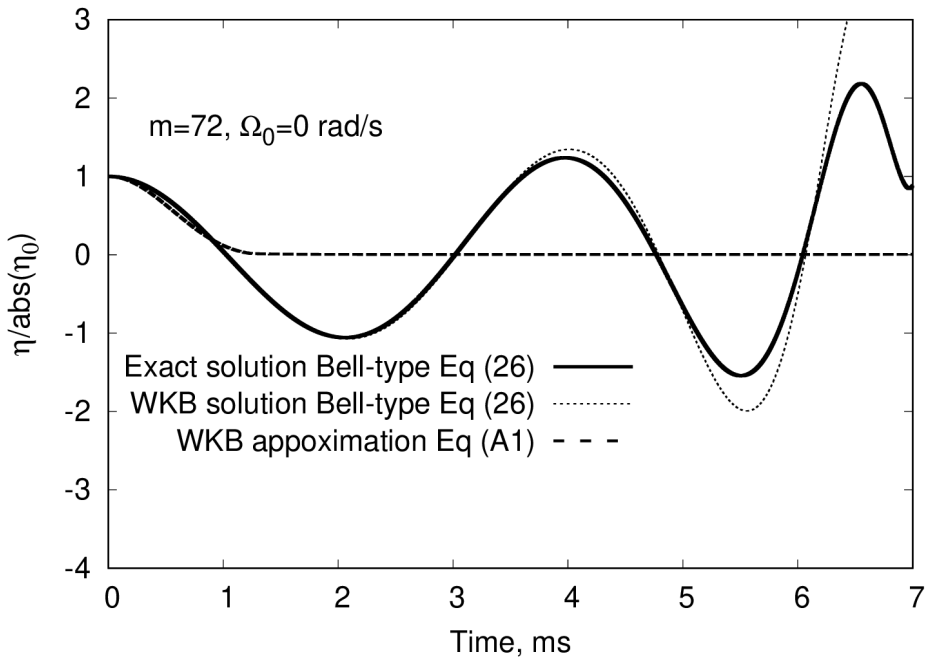
m=72, Ω0=0 rad/s
Exact solution Bell-type Eq (26)
WKB solution Bell-type Eq (26)
WKB appoximation Eq (A1)
η/abs(η0)
Time, ms

(c)

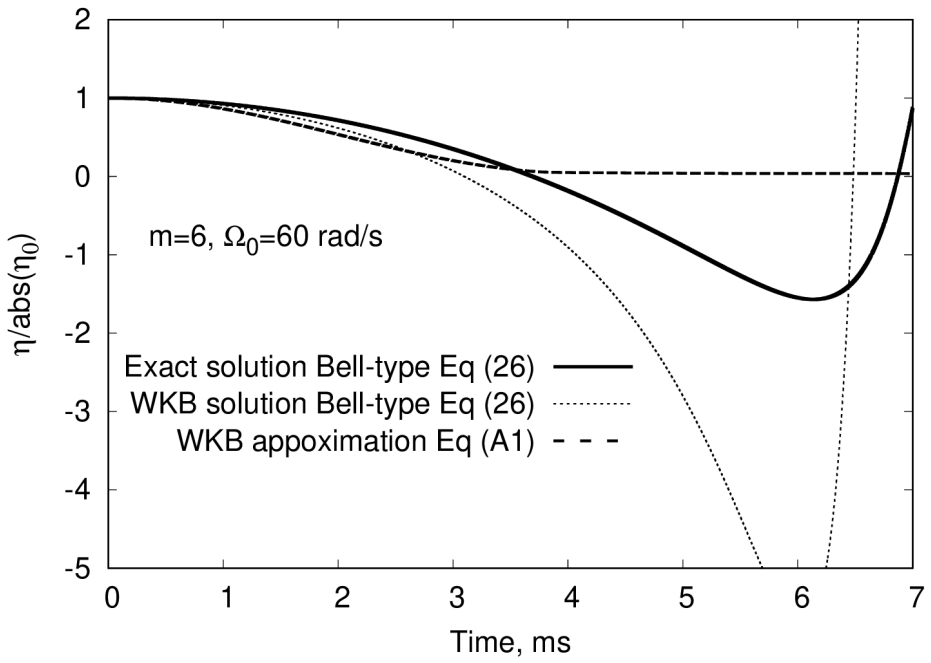

(d)

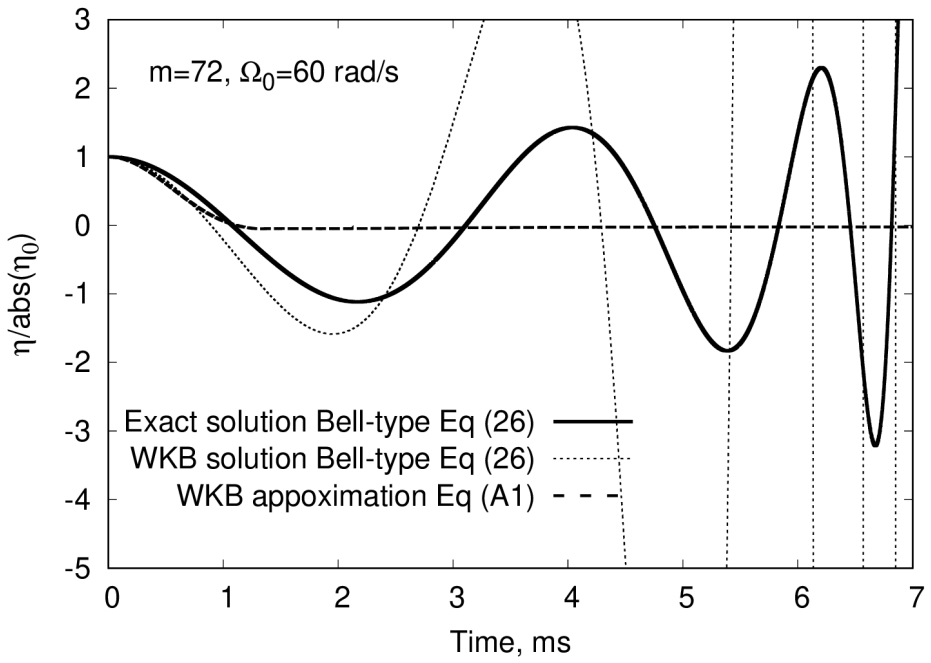

Figure 11: Time developments of perturbation amplitude normalised by its initial absolute value as predicted by the Bell-type linear stability Eq (26), its WKB approximation of an exponential solution and the WKB approximation of Appendix A for (a) m=0, Ω_0=0 rad/s, (b) m=72, Ω_0=0 rad/s, (c) m=6, Ω_0=60 rad/s and (d) m=72, Ω_0=60 rad/s.

Appendix A – Analytical limit for stability during the liner's implosion

For simplicity, the effects of the inner gas disturbance are neglected in the following derivations. This means taking $\mathcal{A}$=1. These effects have small influence on the stability of the imploding liners discussed in Section 3. Requiring the determinant of Eq. (39) to be zero leads to the quadratic equation:

$$a_2\bar{\omega}^2+a_1\bar{\omega}+a_0=0 \quad . \tag{A1}$$

After some patient derivation, one gets:

$$a_2=\rho\left[R_{out}^{m-1}R_{\text{in}}^{-m}+R_{out}^{-(m+1)}R_{\text{in}}^{m}\right] \quad , \tag{A2}$$

$$a_1=i\rho(m-1)u_r^0\left[R_{out}^{m-1}R_{\text{in}}^{-(m+1)}-R_{out}^{-(m+1)}R_{\text{in}}^{m-1}\right] \quad , \tag{A3}$$

$$a_0=m\left(\frac{\partial p^0}{\partial r}+\rho u_r^0\frac{\partial u_r^0}{\partial r}\right)\left[R_{out}^{-(m+1)}R_{\text{in}}^{m-1}-R_{out}^{m-1}R_{\text{in}}^{-(m+1)}\right] \quad , \tag{A4}$$

where in the derivation of a_1 the following expression was used $\partial u_r^0/\partial r=-u_r^0/r$, due to continuity.

One can see that $a_2>0$, and $a_0<0$ if $\partial p^0/\partial r+\rho u_r^0\partial u_r^0/\partial r>0$. The imaginary part of a_1 is always negative during implosion since $u^0_r<0$ and zero at the turnaround point. Hence, a negative effective centripetal acceleration is a sufficient condition for stability at the turnaround point. Assuming a very thick liner, i.e. $R_{out}>>R_{in}$ the solution of Eq. (A1) is;

$$\bar{\omega}=\frac{1}{2}\left[-\frac{i(m-1)u_r^0}{R}\pm\sqrt{\frac{-(m-1)^2(u_r^0)^2}{R^2}+\frac{4m}{R}\left(u_r^0\frac{\partial u_r^0}{\partial r}+\frac{1}{\rho}\frac{\partial p^0}{\partial r}\right)}\right] \quad . \tag{A5}$$

Thus it is sufficient to require $\partial p^0/\partial r+\rho u_r^0\partial u_r^0/\partial r>0$ during implosion ($u^0_r<0$) in order to avoid a negative imaginary part of $\bar{\omega}$ that will lead to instability by this WKB approximation. Taking that $\partial u_r^0/\partial t=(dR_{\text{in}}/dt)^2/R_{\text{in}}+d^2R_{\text{in}}/dt^2$ at $r=R_{in}$ leads by Eq. (1) to a stability condition during implosion;

$$a_t=\frac{d^2R_{\text{in}}}{dt^2}-\frac{(u_\theta^0)^2}{R_{\text{in}}}<-\frac{(dR_{\text{in}}/dt)^2}{R_{\text{in}}} \quad . \tag{A6}$$

If the liner does not implode Eq. (A6) is automatically fulfilled. One should note that requiring angular momentum conservation for the unperturbed motion also fulfils the Rayleigh criterion for centrifugal stability of a non-imploding liner $d(\Omega r^2)/dr\geq 0$ (Drazin & Reid, 2004).

Appendix B – WKB approximation for the inner rotating gas perturbation

It is assumed that the Mach number of the perturbation defined as $|\omega| R_{in}/(m c_{in})$ is small, where c_{in} is the speed of sound in the gas. In all cases studied in Section 3, this perturbation Mach number was found to be smaller than 0.1 Hence, the governing equation for the perturbation is the Poisson equation as for the perturbation in the liner. The velocity potential of the perturbation in the inner gas is taken as

$$\phi = A_{in} r^m e^{i(m\theta+\omega t)} \ , \ m>0 \ . \tag{B1}$$

The kinematic condition from Eq. (20) at $r=R_{in}$ when applied to the inner gas perturbation and taking the same Ω_{in} as of the liner:

$$m A_{in} R_{in}^{m-1} = \left(i\overline{\omega} - \frac{\partial u_{in,r}^0}{\partial r} \right) \eta \ , \tag{B2}$$

while the kinematic condition on the side of the liner yields:

$$m A R_{in}^{m-1} - m B R^{-(m+1)} = \left(i\overline{\omega} - \frac{\partial u_r^0}{\partial r} \right) \eta \ . \tag{B3}$$

The dynamic boundary condition of Eq. (22) becomes:

$$-A\rho\left(i\overline{\omega} + \frac{m u_r^0}{R_{in}} \right) R^m - B\rho\left(i\overline{\omega} - \frac{m u_r^0}{R_{in}} \right) R^{-m} + A_{in}\rho_{in}\left(i\overline{\omega} + \frac{m u_r^0}{R_{in}} \right) R^m + \left(\frac{\partial p^0}{\partial r} - \frac{\partial p_{in}^0}{\partial r} \right) \eta = 0 \ . \tag{B4}$$

Substituting Eqs. (B2) and (B3) into Eq. (B4) will lead to an equation that symbolically can be written as $Ad_{21}+Bd_{22}=0$, thus replacing the expressions for d_{21} and d_{22} in Eqs. (41) and (42) respectively, that were derived when neglecting the effect of the inner gas disturbance. If that effect is to become significant, the inner gas density ρ_{in} should be at the same magnitude as of the liner's density ρ. This may happen at late time stages of the implosion when $R_{out} >> R_{in}$. Hence, it is reasonable to assume the liner is infinitely thick by taking A=0 in the equations above. It will lead to a quadratic equation in the form of Eq. (A1) where

$$a_2 = 1 + \frac{\rho_{in}}{\rho} \ , a_1 = i\left(1 + \frac{\rho_{in}}{\rho} \right) \frac{d R_{in}}{dt} \frac{(m-1)}{R_{in}} \ , \tag{B5}$$

and

$$a_3 = \left(1 + \frac{\rho_{in}}{\rho} \right) \frac{m}{R_{in}^2} \left(\frac{d R_{in}}{dt} \right)^2 - m\left(1 - \frac{\rho_{in}}{\rho} \right) \left(\Omega_{in} - \frac{1}{R_{in}} \frac{d^2 R_{in}}{dt^2} \right) \ . \tag{B6}$$

Inside the liner, $u^0_r = dR_{in}/dt \ R_{in}/r$ to yield incompressibility, and inside the gas, $u^0_{in,r} = dR_{in}/dt \ r/R_{in}$ to yield a uniform gas density by the continuity equation. Hence by the unperturbed momentum equation for the inner gas one gets $\partial p_{in}^0 / \partial r = \rho_{in}\left(\Omega_{in}^2 - d^2 R_{in}/dt^2 \right)$. Taking $\rho_{in}=0$ will yield the solution of Eq. (A5).